HHS Public Access

Author manuscript

J Magn Reson Imaging. Author manuscript; available in PMC 2022 December 01.

Published in final edited form as:

J Magn Reson Imaging. 2021 December ; 54(6): 1706–1729. doi:10.1002/jmri.27367.

Role of Structural, Metabolic, and Functional MRI in Monitoring Visual System Impairment and Recovery

Jeffrey R. Sims, BS[1], **Anna M. Chen, BS**[1,2], **Zhe Sun, MD**[1,2], **Wenyu Deng, BS**[1], **Nicole A. Colwell, MD**[1], **Max K. Colbert, BS**[1], **Jingyuan Zhu, MD**[1,3], **Anoop Sainulabdeen, PhD**[1,4], **Muneeb A. Faiq, PhD**[1], **Ji Won Bang, PhD**[1], **Kevin C. Chan, PhD**[1,2,5,6,7,*]

[1]Department of Ophthalmology, NYU Grossman School of Medicine, NYU Langone Health, New York University, New York, New York, USA

[2]Sackler Institute of Graduate Biomedical Sciences, NYU Grossman School of Medicine, NYU Langone Health, New York University, New York, New York, USA

[3]Department of Ophthalmology, Beijing Tongren Eye Center, Beijing Tongren Hospital, Capital Medical University, Beijing, China

[4]Department of Surgery and Radiology, College of Veterinary and Animal Sciences, Kerala Veterinary and Animal Sciences University, Thrissur, India

[5]Department of Radiology, NYU Grossman School of Medicine, NYU Langone Health, New York University, New York, New York, USA

[6]Neuroscience Institute, NYU Grossman School of Medicine, NYU Langone Health, New York University, New York, New York, USA

[7]Center for Neural Science, College of Arts and Science, New York University, New York, New York, USA

Abstract

The visual system, consisting of the eyes and the visual pathways of the brain, receives and interprets light from the environment so that we can perceive the world around us. A wide variety of disorders can affect human vision, ranging from ocular to neurologic to systemic in nature. While other noninvasive imaging techniques such as optical coherence tomography and ultrasound can image particular sections of the visual system, magnetic resonance imaging (MRI) offers high resolution without depth limitations. MRI also gives superior soft-tissue contrast throughout the entire pathway compared to computed tomography. By leveraging different imaging sequences, MRI is uniquely capable of unveiling the intricate processes of ocular anatomy, tissue physiology, and neurological function in the human visual system from the microscopic to macroscopic levels. In this review we discuss how structural, metabolic, and functional MRI can be used in the clinical assessment of normal and pathologic states in the anatomic structures of the visual system, including the eyes, optic nerves, optic chiasm, optic tracts, visual brain nuclei, optic radiations, and visual cortical areas. We detail a selection of recent clinical applications of MRI

[*]Address reprint requests to: K.C.C., Departments of Ophthalmology and Radiology, NYU Grossman School of Medicine, NYU Langone Health, New York University, 222 E 41st Street, Room 460, New York, NY, USA. chuenwing.chan@fulbrightmail.org.

at each position along the visual pathways, including the evaluation of pathology, plasticity, and the potential for restoration, as well as its limitations and key areas of ongoing exploration. Our discussion of the current and future developments in MR ocular and neuroimaging highlights its potential impact on our ability to understand visual function in new detail and to improve our protection and treatment of anatomic structures that are integral to this fundamental sensory system.

THE VISUAL SYSTEM includes both ocular and neuroanatomy. Recent research has suggested that many visual impairments affect the entire visual system. In addition, their severity cannot be predicted solely via ocular imaging or brain imaging alone.[1–3] This suggests the need for a more in-depth understanding of pathogenesis at a systematic level, rather than individual anatomic structures alone. Whereas other imaging modalities are often limited to specific uses in evaluating single aspects of visual impairment in an anatomical structure, magnetic resonance imaging (MRI) can be employed to assess structure, metabolism, and function throughout the visual pathways. Here, we briefly introduce the key anatomical components of the visual system, as well as relevant MRI techniques in examining the pathology and recovery of these tissues. We then detail specific imaging considerations and a selection of recent clinical applications for MRI in each of the major anatomic regions, along with new developments that are being actively explored. Specific MRI parameters for several studies in each anatomic region can be found in Table 1.

INTRODUCTION TO VISUAL SYSTEM ANATOMY

The mammalian visual system comprises two eyes and their projections along the brain's visual pathways (Fig. 1). The eye is an oblong sphere located within the orbit of the skull, which also houses the extraocular muscles, cranial nerves II–VI, blood vessels, and fat. The walls of the eye can be divided into three major tissue layers: fibrous, vascular, and neural. The outer protective fibrous layer includes the opaque, dense sclera and the transparent cornea, through which light enters the eye. The vascular uveal layer comprises the iris, which controls the size of the pupil; the ciliary body, which produces aqueous humor; and the choroid, which contains smaller blood vessels supplying the eye. The lens sits at the center behind the iris and attaches to the ciliary body via suspensory ligaments. It refracts incident light to focus an image onto the retina. Finally, the neural layer consists of photoreceptors and other neurons that form the retina. Light passes through the inner retinal layers to activate photoreceptors, that is, rods and cones, in the outer retina. This information is then refined as it passes along neurons back to the retinal ganglion cells in the inner retinal layer, and the ensemble of retinal ganglion cell axons projects to the brain as the optic nerve. Important regions of the retina include the optic nerve head, where the retinal ganglion cell axons exit the eye, and the macula lutea, a pigmented area near the center of the retina. The fovea centralis, located at the center of the macula, has the highest concentration of cones in the retina and maximal visual acuity.

The optic nerve is an extension of the diencephalon (ie, a part of the central nervous system) and consists of retinal ganglion cell axons and glial cells. Its major divisions include the

intraocular (within the eye), intraorbital (within the orbit), intracanalicular (as it passes through the skull), and intracranial/cisternal (from the skull's cistern to the optic chiasm) segments. The optic chiasm, located ~10 mm above the pituitary gland, is the anatomical meeting point of the two optic nerves, where the nasal fibers of each nerve decussate.[4] Two optic tracts arise from the chiasm, each containing nasal fibers from the contralateral optic nerve and temporal fibers from the ipsilateral optic nerve. Therefore, each optic tract carries information from the contralateral visual world. The optic tracts course around the cerebral peduncles to reach the thalami, where retinal ganglion cell axons synapse onto the lateral geniculate nuclei (LGN). The LGN are the primary relay centers along the visual pathway. They can also integrate multisensory information such as vestibular stimuli, as well as cortical feedback. The superior colliculi, located in the rostral midbrain, and the pulvinar, located in the thalamus, also receive input from the optic tracts and play a role in coordinating head and eye movement in response to visual stimuli, as well as in unconscious threat perception and facial recognition. Other visually relevant brain structures include the hypothalamic suprachiasmatic nucleus that regulates sleep/wake cycles and the pretectum of the midbrain, which are less well characterized. The optic radiations are geniculocalcarine fibers projecting from the LGN to the primary visual cortex (V1). They are divided in both hemispheres into inferior, central, and superior fascicles.[5] The inferior fascicles (aka, Meyer's loop) process superior visual field information and can be found in the temporal lobes, while the superior fascicles process inferior visual field information and can be found in the parietal lobes. The optic radiations synapse onto V1 along the calcarine fissure of the occipital lobe. Information passes from V1 to higher-order visual areas in the occipital lobe, as well as the temporal and parietal lobes, for more complex processing of visual information.

INTRODUCTION TO MRI TECHNIQUES FOR THE VISUAL SYSTEM

MRI is a noninvasive imaging modality that is clinically useful in evaluating various forms of neuropathology such as inflammation, demyelination, trauma, malignancy, and ischemia along the brain's visual pathway.[6] Furthermore, its robust spatial resolution in comparison to other noninvasive imaging modalities (eg, ultrasound) enables clinicians and researchers to examine the entire visual system in a single setting. MRI allows for the imaging of biological tissues by generating a strong magnetic field that causes protons within the tissues to align, and then exciting a specific subset of protons within the desired anatomy using a radiofrequency current.[7] Most clinical MRI machines have field strengths of 1.5–3T. Higher field strengths (7T or greater), while not widely used outside of research settings, are being increasingly utilized in clinical practice. Advantages of high-field imaging include increased image resolution at a higher signal-to-noise ratio (SNR), but there are safety tradeoffs to consider at higher fields, such as heating of tissue and peripheral nerve stimulation.[8,9] Image quality can also be affected by artifacts due to voluntary and involuntary patient movement, magnetic field inhomogeneities, and chemical shift from the tissue itself, which has required the development of specialized hardware and techniques.[10] Here, we introduce MRI techniques that are used to evaluate the visual system.

Structural MRI

Structural MRI uses high-resolution MRI sequences to image tissue anatomy. Standard structural MRI sequences used in ophthalmology include T_1- and T_2-weighted imaging.[7] Magnetization preparation modules can be appended to these sequences to improve tissue contrast; the fluid-attenuated inversion recovery (FLAIR) sequence generates a T_2-weighted image with greatly reduced signal from fluid, facilitating recognition of abnormalities and improved differentiation of structures.[11] However, structural MRI cannot be used to assess the functional properties of a system or identify microstructural abnormalities.

Administration of contrast agents can improve the diagnostic accuracy of structural MRI sequences. Gadolinium-based contrast agents (GBCAs) are passive paramagnetic ion complexes that can shorten the T_1 (longitudinal) and T_2* (transverse) relaxation times of neighboring water protons. T_1-weighted images after gadolinium administration are often used to distinguish tumors from inflammation and edema, or to highlight vessels for angiography. GBCAs have also been used in research settings, such as in studies demonstrating decreased cerebrospinal fluid clearance in idiopathic normal pressure hydrocephalus.[12–14] Manganese, conversely, is an active paramagnetic contrast agent that enhances brain tissue in T_1-weighted images. It acts as both an anterograde tract tracer and a calcium analog, allowing for the visualization of the white matter tract and neuronal activity. Although chelated manganese (eg, Mn-DPDP) has been used in clinical imaging of the pancreas, ophthalmological use of manganese-enhanced MRI is primarily limited to animal studies due to toxicity concerns.[15]

Diffusion MRI

Diffusion imaging provides information on a microstructural scale by measuring the average displacement of molecules within a voxel of tissue. Two common types are diffusion-weighted imaging (DWI), which measures water diffusivity in a single direction and offers the basic building blocks for more advanced diffusion models; and diffusion-tensor imaging (DTI), a method that primarily exploits anisotropic diffusion in the microscopic environment along multiple directions within a voxel.[16] DWI can produce an apparent diffusion coefficient (ADC) map displaying different rates of diffusion within different tissues. Water molecules moving faster and with less restriction (eg, cerebrospinal fluid) produce more signal loss in DWI. In contrast, water molecules moving slower in more restrictive environments (eg, gray and white matter) result in relatively lower signal loss in DWI. Thus, the types of signal contrast produced by DWI sequences provide global information about areas of unusually restricted diffusion, such as in ischemic stroke, tumors, or lesions, or areas of abnormally high diffusion, as in the case of vasogenic edema.[16]

In situations where DWI's scalar assessment of diffusion is insufficient, DTI is able to extract more specific diffusion properties such as the magnitude and principal direction (ie, the direction of the fastest diffusion) within the voxel. Constraints (eg, organized fiber tracts, resulting in anisotropic motion) or lack thereof (eg, stroke, giving rise to isotropic motion) provide information about microstructural injury and the effects of disease progression. DTI data provide the means to calculate multiple parametric maps to evaluate the degree of anisotropy and other signal properties. Fractional anisotropy (FA) and mean diffusivity

(MD) are the most widely used parameters in clinical radiology; axial diffusivity (AD) and radial diffusivity (RD) provide additional information. The FA map outlines the principal diffusion direction and can be used in conjunction with DWI and ADC maps to help clinicians differentiate types of edema, tumors, and cysts. In research, diffusion imaging is especially valuable for analyzing white matter tracts and structural connectivity.[17]

Functional MRI

Blood oxygenation level-dependent (BOLD) imaging, also known as BOLD functional MRI (fMRI), detects changes in paramagnetic deoxyhemoglobin and is capable of reflecting neuronal states based on hemodynamic activity, such as blood flow, blood volume, and the oxygenated hemoglobin concentration in tissues of interest.[18] Brain activity can be measured during both task performance (ie, task-based fMRI), and task absence (ie, resting-state fMRI). In task-based fMRI, activated brain areas corresponding to a stimulus can be inferred based on signal changes from the BOLD baseline, which can be designed to investigate a particular cognitive function. In resting-state fMRI, simultaneous BOLD fluctuations are measured to identify the BOLD time course correlation between a region of interest (ROI, or seed voxels) and the rest of the brain. In addition to seed-based analysis, other commonly used analysis methods include independent component analysis, graph theory, clustering algorithms, and multivariate pattern classification.[19] Pertinent concerns in using fMRI include poor temporal resolution due to hemodynamic response lag, which must be accounted for during post-processing, and distortion along the air–brain and air–eye interfaces due to field inhomogeneity.[20]

Magnetic Resonance Spectroscopy

MR spectroscopy (MRS) is another quantitative technique often used to measure a spectrum of brain metabolites within a given voxel, illustrating the presence and respective concentration of these substances. The most common metabolites of interest for proton MRS include N-acetylaspartate (NAA), a marker for neuronal integrity; creatine (Cr), which reflects energy metabolism; choline (Cho), a marker for cell membrane turnover; glutamate, an excitatory neurotransmitter; glutamine, which cycles with glutamate in the brain; myo-inositol, a glial marker; lactate, a marker for anaerobic metabolism; and gamma-aminobutyric acid (GABA), an inhibitory neurotransmitter. Low NAA often indicates neuronal injury, while high choline indicates high cell membrane turnover (eg, neoplasm, demyelination, gliosis).[21] Ratios of metabolites to the relatively stable creatine or water signals are often performed to account for systematic fluctuations between experimental sessions. These ratios can reveal biochemical and metabolic changes that may occur prior to visible morphological damage, which can be detected via structural imaging. Further research examining metabolic and functional coupling may provide insight for targeted therapies to counteract metabolic dysfunction.

APPLICATIONS OF MRI FOR THE EYE AND ORBIT

The adult human eye, on average, has an anterior–posterior diameter of ~24 mm and a volume of 6–7 mL.[22,23] As described above, the eye wall has fibrous, vascular, and neural layers that play specific roles in communicating visual information to the brain. The retina is

involved in processing and encoding this information and has an average area of ~1100 mm^2 and thickness of ~250 μm, though its thickness varies at different anatomical positions and often changes under pathological conditions.[24] The orbit, which houses the eye, muscles, nerves, fat, and other associated tissues, is a conical structure with a depth of 4–5 cm and volume of ~30 mL.[25] While the majority of ocular MRI techniques used in clinical practice are structural, we will touch upon several multiparametric experimental techniques for ocular imaging that are being actively explored.

Imaging Techniques

Imaging of the eye often requires specific hardware and sequences. While standard head coils can capture larger ocular structures, specialized receiver coils like a single surface coil or four-channel eye coils significantly increase SNR. For example, a surface microscopy coil with a 47-mm inner diameter at 1.5T can produce high-resolution scans to visualize details of the eyelid, anterior chamber angle, and ocular layers.[26] At 7T, 5-cm diameter receive-only surface coils have been used with either a quadrature volume coil for transmission or a 2×2.3 cm^2 single-loop oval coil. Beenakker et al also designed a three-channel receive microcoil array for in vivo ocular scans to characterize tumor heterogeneity and geometry in patients with uveal melanomas[27] (Fig. 2a–c). However, increased sensitivity can result in enhanced motion artifacts, which present a particular challenge when scanning the eye. Some methods to account for eye motion include image acquisition timed after blinking or eye trackers.

Applications

ORBITAL INFLAMMATION AND LESIONS.—Orbital inflammation can be difficult to diagnose with computed tomography and ultrasonography alone, as more invasive testing is often required to rule out infection or malignancy. MRI, however, is capable of examining these soft-tissue structures and, in combination with clinical data, may help prevent unnecessary biopsies. The imaging protocol ideally includes T_1- and T_2-weighted sequences with and without fat suppression, T_1-weighted sequences with postcontrast fat suppression, and DWI.[28] Contrast enhancement can provide important etiological clues, as inflammatory lesions often enhance homogeneously, while infections and tumors typically have more heterogeneous patterns. DWI can be particularly helpful in differentiating benign and malignant lesions; inflammatory lesions are generally less water-restricting than malignant tumors and thus have higher ADC values (Fig. 2d). Bacterial infections may contain pus, resulting in specific areas of nonenhancement and water restriction.[28]

THYROID EYE DISEASE.—One of the most common clinical indications for orbital MRI is suspected thyroid eye disease. In patients with hyperthyroidism due to Graves' disease, autoantibodies against the thyroid-stimulating hormone receptor crossreact with antigens in the orbit, causing inflammatory mediators to activate orbital fibroblasts that proliferate and lead to extraocular muscle swelling, orbital fat expansion, and fibrosis.[29] While computed tomography is often the initial imaging modality in suspected thyroid-associated orbitopathy, the benefits of MR include better assessment of orbital fat and the optic nerve without ionizing radiation. T_1-weighted images typically show isointensity of the extraocular muscles with higher signal in the setting of fatty infiltration. Conversely,

T_2-weighted images can show hyperintensity.[30] Short-TI inversion recovery (STIR) is particularly useful for nulling signals from fat tissue in the orbital region. Since signal intensity of the extraocular muscles has been shown to correlate with clinical disease activity scores, serial STIR imaging can be employed to identify active orbital inflammation in chronic thyroid eye disease[30,31] (Fig. 2e,f).

OCULAR TUMORS.—Intraocular tumors, the most common being uveal melanoma, are diagnosed both clinically and via various imaging modalities, including ultrasound, optical coherence tomography, and fluorescein angiography. However, recent multiparametric ocular protocols were developed for 3T MRI in evaluating uveal melanomas, using eye coils and relevant anatomical, functional, and diffusion sequences to differentiate benign from malignant lesions and predict treatment outcomes.[32] Additionally, acquisitions at 7T yield more accurate measurements of tumor size than ultrasound,[33] which could better inform clinical decision-making, including the choice of enucleation (ie, surgical removal of the eye), eye-preserving therapy, or brachytherapy with radioactive implant (Fig. 3a). Unlike ultrasound and optical coherence tomography, MRI is unaffected by ocular media opacities, such as cataracts, vitreous hemorrhage, retinal detachment, or silicone oil tamponade.[34] This advantage enables high-resolution imaging for follow-up monitoring and treatment planning in uveal melanoma patients.[35]

In contrast to uveal melanoma, definitive treatment for retinoblastoma—the most common intraocular childhood tumor—relies heavily on MRI. However, clinical MRI field strengths are incapable of detecting tumor extent (eg, choroidal or optic nerve invasion), which is essential in deciding if eye-preserving therapy is feasible or if adjuvant systemic chemotherapy is necessary. Ultrahigh-field MRI of retinoblastoma samples performed ex vivo at 9.4T and 17.6T have been capable of detecting small morphological details, such as patterns of tumor tissue, vessels, and areas of necrosis, which correlated well with histopathological findings in the same sample. These observations demonstrate the potential of MRI for more accurate tumor staging at higher magnetic field strengths[36] (Fig. 3b).

BLOOD–OCULAR BARRIER INTEGRITY.—Similar to the blood–brain barrier (BBB) that surrounds the brain, the blood–ocular barrier (BOB) protects the eye by regulating the flow of molecules and potentially toxic agents out of the blood-stream and into the ocular tissues/compartments. The two primary components of the BOB are the blood–aqueous barrier and the blood–retinal barrier. While largely protective, the BOB also likely accounts for challenges in the systemic administration of medications for intraocular tissues.[37] Certain conditions are known to be capable of causing a breakdown of the BOB, including ocular hypotony and sources of inflammation and injury, including trauma, uveitis, vascular disorders, intraocular tumors, and systemic diseases like diabetes.

Gadolinium leakage into ocular structures (GLOS) has been observed in a number of conditions, including optic neuritis and stroke[38,39] (Fig. 3c). A recent retrospective study evaluating GLOS on postcontrast FLAIR MRI in acute ischemic strokes found that GLOS was evident in the majority of patients, often bilaterally, and that rapid diffuse GLOS significantly correlated with larger infarct size and increased BBB permeability, whereas chronic cerebral microvascular disease was associated with delayed GLOS. These results

may have implications regarding the mechanisms of BOB and BBB disruption in cerebral ischemia, and ophthalmic markers of BOB disturbances may offer a way to more easily measure BBB damage.[38] Dynamic contrast-enhanced MRI (DCE-MRI), which can measure T_1-weighted changes over time following contrast administration, has also been used in retinovascular studies to evaluate blood–retinal barrier damage in diabetes[40] (Fig. 3d). In patients with diabetic macular edema, there were significant abnormalities in MRI signal enhancement, and some patients who had not yet developed diabetic retinopathy showed supernormal oxygenation responses (Fig. 3e,f). These findings suggest that MRI is capable of detecting subtle changes in retinovascular function prior to clinical signs of diabetic retinopathy and may provide utility in evaluating the effectiveness of treatment.[40]

Future Directions

MRI techniques that are currently in development may offer new ways to image the intricate structures and physiology of the eye. Preclinical studies have explored the magic angle effect, which produces tissue enhancement when the angle between the MRI's main magnetic field and fibers of collagenous tissue is 54.7°. This effect could likely be exploited in future human research for microstructural imaging of the corneoscleral shell under such conditions as aging, myopia, keratoconus, and glaucoma.[41,42] While challenges of resolution and eye motion have limited the utility of standard MRI for retinal pathology, which is more frequently assessed via optical coherence tomography and stereoscopic fundus photography, non-Cartesian sampling techniques like zero-echo time imaging have made retinal MRI more feasible.[43] Quench-assisted MRI, which can detect excessive free radical production without exogenous contrast agents, has also shown early promise.[44] There are also ongoing studies exploring targeted MRI of the vitreous, including diffusion, MRS, and oximetry imaging.

APPLICATIONS OF MRI FOR THE OPTIC NERVE, CHIASM, AND TRACT

The optic nerves (cranial nerve II), which are ~40-mm long structures composed of retinal ganglion cells and glial cells, traverse posteriorly from the orbit to the optic chiasm via the optic canal, a foramen of the sphenoid bone. These cranial nerves are susceptible to various pathologies including inflammation, trauma, and malignancy. The optic chiasm is located at the base of the brain, inferior to the hypothalamus and superior to the sella turcica, which houses the pituitary gland. This structure can also be affected by inflammation or compressed via mass effect from pituitary tumors. Anatomical, diffusion, and fMRI can be used to help assess the integrity of these structures.

Imaging Techniques

The relatively small size and the presence of surrounding orbital fat makes the optic nerve somewhat difficult to characterize via conventional MRI. As described for eye and orbit imaging, surface coils are often used to better evaluate these structures.[4,45] For example, one group designed a 20-channel phased array coil for improved visualization of the optic nerve, with greater imaging depth, accelerated scanning, and preservation of image quality via parallel imaging reconstruction methods.[46]

Applications

DEMYELINATION.—Demyelination of the visual pathway can occur as a result of various underlying conditions. It is not uncommon for demyelinating optic neuritis to be the presenting symptom in multiple sclerosis or neuromyelitis optica. Neuromyelitis optica is typically bilateral, involves nearly half the length of the optic nerve, and often extends posteriorly to involve the chiasm.[47] However, bilateral optic nerve involvement does not rule out multiple sclerosis. ADC quantification from DWI has been shown to differentiate multiple sclerosis and neuromyelitis optica with an accuracy of 76.7%[48] (Fig. 4a,b). Increasing evidence also suggests a demyelinating component in glaucoma. DTI studies have shown decreased FA and increased RD in the optic nerves and optic tracts in glaucoma, with degeneration progressing in a Wallerian-like fashion[49,50] (Fig. 4d). While demyelination and axonal degeneration have been shown to correlate with increased RD and decreased AD, respectively, other processes such as gliosis and inflammation may confound these DTI metrics.[51] Whereas DTI is useful for assessing microstructural damage, fMRI is useful for evaluating functional deterioration and recovery in optic nerve damage by measuring BOLD activation distally in the visual cortices.[52]

TRAUMA.—In trauma patients sustaining blunt force injuries to the head, there is concern for indirect traumatic optic neuropathy, which can result in permanent visual deficits secondary to axonal degeneration. Since conventional imaging modalities are unable to detect axonal degeneration, it is important to establish a means to assess axonal integrity. Results from DTI studies of indirect traumatic optic neuropathy have indicated decreased FA and AD, and increased RD in the injured optic nerves, suggesting the potential utility of this technique in ruling out such conditions[53,54] (Fig. 4c).

TUMORS.—MRI is often used to evaluate neoplasms involving or surrounding the visual pathway, such as optic nerve hypertrophy seen in optic nerve gliomas and nerve sheath meningiomas[55] (Fig. 4e). Although MRI is an essential tool in the management of pituitary tumors that compress the optic chiasm, causing bitemporal hemianopia, currently available imaging methods perform suboptimally in predicting postoperative visual outcomes.[56]

Future Directions

While conventional anatomical MRI and DWI have an established place in evaluating the integrity of the optic pathway, significant limitations remain. For example, imaging of the eye is often done statically, with patients asked to fix their gaze to minimize movements that would create artifacts. However, since involuntary eye and optic nerve motion may provide valuable information about oculomotor function in health and disease, dynamic imaging of the eye using a golden angle radial sequence has shown promise.[57] This sequence was found to be not only motion-robust, but also temporally advantageous, with an ~15-second acquisition time. On the other hand, accurate diffusion measures of the optic pathway often suffer from low SNR and long scan times due to the application of strong gradients at high resolutions in many encoding directions.[58] One study explored the efficacy of a reduced field-of-view (FOV)-DTI sequence for imaging the optic nerve, with results suggesting improved SNR over a relatively short scan time compared to conventional DTI.[59] For DWI, many small-FOV sequences have demonstrated reduced image distortion and improved

resolution of the optic nerve.[45] Higher-order imaging modalities have also been designed for deeper exploration into the microstructure and biophysical relevance. For example, diffusion basis spectrum imaging and the extended diffusion kurtosis imaging technique called the white matter tract integrity model can separate intra- and extra-axonal volumes for quantification, and can provide measures such as axonal water fraction and tortuosity of the extra-axonal space.[51,60] Combining this greater level of detail with histologic data will allow for more accurate characterization of tissue architecture.

APPLICATIONS OF MRI FOR THE VISUAL BRAIN NUCLEI

The importance of the LGN is increasingly being recognized, given their role as the major synaptic crossroads of the visual system. The LGN, which are ~60–160 mm^3 in size bilaterally, receive anterograde and retrograde input from the retina and cortex, respectively, as well as from other regions. As such, the LGN effectively serves as a "common denominator" for pathology affecting structures along the entire visual pathway. Other subcortical brain structures known to have roles in the visual system include the superior colliculi, pulvinar, suprachiasmatic nucleus, and pretectum, as well as deep gray nuclei in top-down projections to V1.[61] Although the visual nuclei are not routinely imaged as the standard of care for individual disease, the clinical utility of MRI to evaluate the structure, function, and metabolism of these structures is under active investigation.

Imaging Techniques

MRI of the LGN has been limited by their small size and location adjacent to other functionally distinct nuclei, precluding the ability to reliably differentiate the LGN from surrounding structures. Despite the capabilities of 7T MRI, adoption of this higher field strength has not become universal practice, contributing to protocol variability. Attempts at improving image quality have yielded a number of sequencing methods that, while elegant in concept, are generally time-consuming and cumbersome in clinical practice, albeit with some promising exceptions.[62]

Applications

GLAUCOMA.—Previously thought to be a primarily ocular disease, glaucoma is a neurodegenerative disorder affecting the optic nerve, often in the setting of elevated intraocular pressure.[63] It was recently demonstrated that glaucoma is associated with structural and functional changes among numerous brain networks, potentially compromising postural control and visuomotor coordination.[64] New data suggest that a combination of imaging findings may help in early diagnosis of glaucoma. Structural MRI of glaucoma patients consistently reveals smaller LGN size and height compared to healthy subjects[65,66] (Fig. 5a–d). However, association of LGN size with other common clinical features, such as disease severity, has been less straightforward, with studies reporting seemingly contradictory results.[65] Multiple studies have shown a correlation between reduced LGN volume and retinal layer thinning on clinical imaging, but the specific layer with decreased thickness has been disputed.[67,68] LGN volume is similarly associated with optic tract FA values on DTI, the latter being highly sensitive and specific for glaucoma, further suggesting that MRI findings specific to these structures may indicate glaucomatous

disease.[69] In terms of brain function, high-resolution fMRI has also shown decreased activation localized to both the LGN and superior colliculi in early glaucoma patients. Signal loss on fMRI was specific to magnocellular (M-type) tissue layer loss in the LGN, with no sign of loss of the parvocellular (P-type) tissue layers. This selective response reduction can be detected in the early stages of the disease, increasing the potential diagnostic and prognostic values of these techniques.[70]

In terms of brain metabolism, a recent study utilizing proton MRS identified abnormally low NAA:Cr and Cho:Cr ratios, suggesting neurodegeneration within the LGN and striate cortex of glaucoma patients.[71] Another study identified increased glutamate–glutamine complex to Cr ratios in both the LGN and vitreous of glaucomatous eyes, providing evidence for excitotoxicity as a potential mechanism leading to neuronal apoptosis within structures of the visual system.[72] Additionally, decreased NAA:Cr ratios have been observed in the LGN and vitreous in glaucoma patients, and a similar metabolic disturbance was also observed in a “suspected glaucoma” cohort, suggesting neuronal loss in both groups.[73] While the use of these imaging strategies for diagnostic guidance in suspected glaucoma would address an unmet need in this clinically ambiguous population, this application requires further clinical validation.

AMBLYOPIA AND BLINDNESS.—Amblyopia, a developmental disorder of vision, arises as a result of abnormal input to the visual system during early life. Changes occur at the neuronal level in early visual areas, and affected patients typically have poor visual acuity, contrast sensitivity, and stereopsis.[74,75] fMRI has elucidated the role of LGN in the pathogenesis of this disease, which was previously thought to be primarily cortical in etiology.[76] Using layer-specific LGN imaging, it has been possible to provide evidence for parvocellular-specific dysfunction in these patients.[77] Furthermore, fMRI has shown compensatory subcortical remodeling involving the superior colliculi in individuals with congenital and early-onset blindness. During auditory stimulation in these patients, the superior colliculus becomes recruited by thalamic auditory processing networks that are normally more strongly associated with the inferior colliculus[78] (Fig. 5e–g). Apart from fMRI detection of subcortical dysfunction and cross-modal plasticity, amblyopic patients with isolated visual input to the affected eye demonstrated increased BOLD activity following occlusive therapy,[79] highlighting the potential application of fMRI for treatment monitoring.

Future Directions

Structural MRI may measure LGN volume as a biomarker for cumulative insult to the visual system. Tissue layer-specific fMRI may also confirm damage associated with loss of function in the subcortical visual brain nuclei. These patterns have recently been identified for diseases such as Alzheimer’s disease, Parkinson’s disease, and schizophrenia.[70] Lastly, metabolic imaging may assist with confirmation of diagnosis in equivocal glaucoma cases and help to elucidate the mechanisms driving glaucoma pathogenesis. This insight could guide the development of therapeutic strategy on eye-vs. brain-related factors as appropriate.

APPLICATIONS OF MRI FOR THE OPTIC RADIATION

The optic radiations are dense white matter bundles, with an average length of ~100 mm, that exit from LGN and end at V1 along the calcarine fissure of the occipital lobe.[80] Identifying and tracking the optic radiations, particularly Meyer's loop, are of significant importance in neurosurgical interventions. Additionally, measuring the appearance, properties, and metabolic abnormalities of these structures can provide insight regarding visual information transmission defects. The most commonly used clinical MRI modalities for the optic radiations are structural and diffusion imaging. Although conventional morphological imaging sequences are unable to image healthy optic radiation fibers due to the lack of in situ tissue signal contrast, MRI can still be utilized to examine lesions in this region. Several other experimental imaging techniques and construction algorithms are being actively developed as well.

Imaging Techniques

Altered diffusion parameters within the optic radiations have been found in visual field loss, visual pathway tumors, optic neuropathy, retinopathy of prematurity, and cerebral white matter injury.[81–83] DTI can also be utilized to reconstruct the optic radiations and evaluate cerebral connectivity via diffusion tensor tractography, which works by inferring connectivity between neighboring voxels based on diffusion properties. However, tractography of Meyer's loop encounters problems due to crossing fibers and areas of high curvature. To overcome these issues, more advanced DWI sequences and tractography algorithms have been developed, such as high angular resolution diffusion imaging, which uses a constrained spherical deconvolution model in regions of crossing fibers with probabilistic fiber tracking, and takes whole-brain anatomical information into consideration to improve biological accuracy.[84]

Spectroscopy has also proven useful in identifying optic radiation demyelination. While conventional MRI can detect large, clinically symptomatic lesions, abnormalities within normal-appearing white matter may also cause disability.[85] MRS can be applied to quantitatively investigate metabolic changes in areas of demyelination. Decreased NAA and parallel reductions of axonal density have been found in demyelinating plaques. Additionally, choline and myo-inositol have been elevated in reaction to glial proliferation.[86]

Applications

MULTIPLE SCLEROSIS.—In multiple sclerosis, optic radiation damage can occur via primary degeneration, as well as secondary neurodegeneration as a consequence of trans-synaptic mechanisms following injury to the anterior visual pathway. T_2-weighted imaging can reveal lesions of hyperintense signals within the optic radiation region. Recently, enhanced T_2*-weighted angiography demonstrated significant advantages over susceptibility-weighted imaging, including higher SNR and reduced chemical shift artifact. This technique can be applied to better visualize iron decomposition and thickness changes within the optic radiations in multiple sclerosis[87] (Fig. 6a–c). White matter tract reconstruction can also visualize these lesions, especially in the middle part of the optic radiation neighboring the lateral ventricles[88] (Fig. 6d). Quantitatively, DTI studies have

revealed abnormal optic radiation diffusivity in multiple sclerosis, including decreased FA and increased AD, RD, and MD.[89] Furthermore, retinal layer thickness was found to be positively correlated with FA and negatively associated with RD, suggesting propagation of neuronal dysfunction along the visual pathway.

AMBLYOPIA.—DTI can be used to investigate the integrity and connectivity of the optic radiation in amblyopia. Compared to normal-sighted subjects, increased MD was observed in the optic radiation of amblyopic children[90] (Fig. 7a,b). Furthermore, the total number of voxels comprising the posterior optic radiation was found to be reduced in children with amblyopia, indicating optic radiation maldevelopment.[91] FA in the optic radiation of these children was observed to be lower than those in controls and was positively correlated with cortical thickness of vision-related brain regions, suggesting that optic radiation damage in children with amblyopia may be associated with impaired functional networks.[92]

GLAUCOMA.—Glaucoma patients have been shown to have a significantly higher MD and lower FA within the optic radiation compared to control subjects, suggesting compromised white matter integrity.[93] Using whole-brain analysis via tract-based spatial statistics, clusters with significantly lower FA were found in the bilateral optic radiations and the forceps major of glaucoma subjects.[83,94] Concurrently, a positive association between FA of the bilateral optic radiations and retinal nerve fiber layer thickness was observed[94] (Fig. 7c), suggesting associations with disease severity. Consensus has not been reached regarding metabolic changes. A multivoxel proton MRS study reported significant decreases in NAA:Cr and Cho:Cr, indicating neurodegeneration within the geniculocalcarine tracts of glaucoma patients[71] (Fig. 8a–c). Conversely, single-voxel proton MRS studies have not detected significant changes in metabolite concentration within the optic radiation in glaucoma.[95]

PRESURGICAL PLANNING.—The fibers in Meyer's loop pass anteriorly over the roof of the lateral ventricle and then turn backward. Surgeries involving this region, such as epilepsy surgery and tumor resections, may cause contralateral quadrantanopia. Diffusion tensor tractography, using probabilistic algorithms and the constrained spherical deconvolution model, for instance, can enable finer resolution imaging of optic radiation fiber architecture during presurgical planning.[96]

Future Directions

Optic radiation imaging reconstruction can provide important anatomical information for epilepsy surgery. Aside from preoperative tractography, an intraoperative imaging and surgery navigation platform can provide real-time tracking, which may be capable of reducing the severity of visual field deficits and achieving successful seizure remission.[97] Future incorporation of these techniques into routine clinical practice could significantly improve surgical outcomes for these patients.

APPLICATIONS OF MRI FOR THE VISUAL CORTEX AND HIGHER-ORDER VISUAL AREAS

The visual cortex is a collection of areas located in the occipital lobe of the brain, including the striate area (V1, Brodmann area 17) and extrastriate visual areas 2 (V2, Brodmann area 18), 3, 4, and 5 (V3, V4, and V5; all Brodmann area 19). As part of the brain's cerebral cortex, it is an ~1–4 mm thick neural tissue layer.[98] Histological studies have found that the size of V1 varies among healthy individuals and is independent of overall brain size. However, anatomical imaging allows for the accurate estimation of visual cortex volume and surface area. These measures may help uncover differences in dysfunctional relative to normal-functioning systems. The visual cortex can also be delineated using retinotopic mapping, an important method in identifying the spatial distribution of visual field information as well as functional boundaries between higher-order visual brain areas.[99,100]

In the following section, we discuss two visual disorders involving cortical networks. Clinical MRI applications for the visual cortex can range from structural imaging and voxel-based morphometry analysis to more advanced techniques exploring function (BOLD fMRI), neuroarchitecture (DWI/DTI), and metabolism (MRS)[83] (Fig. 8d). These approaches can not only be made sensitive to neurophysiologic abnormalities and help better understand mechanisms of disease, but also be used to explore brain reorganization in rehabilitation or recovery.

Imaging Techniques

Common MRI modalities for studying the visual cortex include both structural (T_1- and T_2-weighted) and functional sequences. DWI/DTI and arterial spin labeling are useful for surgical planning, while additional sequences like susceptibility-weighted imaging and MRS may be included in research. MR angiography is especially important in visual deficits caused by arterial infarction.[101] Since the visual field is divided between the anterior and posterior portions of the calcarine fissure, efforts geared toward retinotopic analysis and cortical mapping have increased to augment surgical planning in brain tumor patients[99,102] (Fig. 9a–d).

Applications

AMBLYOPIA.—As noted, amblyopia is a disorder of the visual system at the neuronal level resulting from poor input[103] (Fig. 9e,f). Conventional amblyopia therapy typically includes eye patching, which covers the preferred eye to force the brain to process signals from the amblyopic eye. While patching can reverse amblyopia at an early age, it is reportedly less effective once this sensitive period has passed.[74,75] Nevertheless, studies have demonstrated that adult visual systems have remarkable plasticity. For example, repetitive visual practice can improve performance on various visual tasks and change the visual system in normal-sighted adults.[104] Recent studies in amblyopia have examined whether extensive visual practice with patching can reverse amblyopia in older children and adults.[74,75,105] Following visual practice, patients showed performance improvement on the trained task, some even having improved visual acuity.[106,107]

Although the mechanisms through which visual perceptual learning can reverse amblyopia in older children and adults are largely unknown, accumulating neuroimaging findings in normal-sighted adults provide substantial information. A number of studies demonstrated that visual perceptual learning is associated with changes in the visual system, from LGN to the visual cortical areas. Previous studies have also shown that the BOLD signal increases in LGN and V1 as a result of visual training.[108,109] Notably, when learning reached its maximum after 5–6 days of training, the BOLD signal returned to baseline.[108] Other studies have demonstrated that the neurochemical environment, measured by the glutamate:GABA ratio, changes with visual training in early visual areas, including V1, V2, and V3.[110] An inhibitory-dominant neurochemical environment in these areas was associated with a stable state of visual perceptual learning, whereas an excitatory-dominant environment was associated with a plastic state.

Some studies have examined plasticity beyond the visual areas. One group found that resting-state BOLD connectivity and directed mutual interaction between trained visual areas and frontal–parietal areas, which are involved in spatial attention, are significantly modified with visual training and that these changes are associated with the degree of learning.[111] Another study examined plasticity during the late phase of learning, after performance reaches a plateau, showing that structural and functional connectivity between V1 and anterior brain areas change along the longitudinal fasciculus in the late phase of visual perceptual learning.[112] These studies suggest that changes occur on a large scale, linking both visual and higher cognitive areas.

Given the above findings, visual training may reverse amblyopia through similar changes in the brain. However, more research is needed to better understand how visual training alters amblyopia, which will eventually contribute to more effective forms of clinical intervention.

HEMIANOPIA.—Hemianopia refers to the complete loss of vision in half of the visual field, caused by unilateral damage to the optic radiation or V1, with etiologies including stroke, traumatic brain injury, and tumor resection[113–115] (Fig. 10a–d). Other diseases, including multiple sclerosis and Alzheimer's disease, may also result in hemianopia due to post-chiasmatic lesions.[116] Behavioral assessments (eg, perimetry testing) are often used to evaluate the extent of visual field loss. Because various pathologies can cause hemianopia, structural MRI can often localize the damaged or affected neuroanatomical regions, aiding in clinical diagnosis[117] (Fig. 10).

Further investigation of cortical function in hemianopic patients with fMRI and diffusion MRI has deepened our understanding of cortical blindness and compensatory reorganization, a potential mechanism of recovery. For example, task-based fMRI reveals cerebral activation and reorganization dependent on the task performed and the side of the occipital lesion.[118] In children with congenital and acquired hemianopia, task-based fMRI also detected reorganization of V1 networks to compensate for the lack of input from the lesioned visual pathway.[119] These fMRI studies not only demonstrate plasticity in the visual system across hemianopia etiologies, but also highlight regions that are important to specific visual processing tasks, which cannot be elucidated by other imaging methods. Additionally, some hemianopic patients exhibit blindsight, where some visual function and response

to stimuli remain without conscious perception. Since the visual cortex is subdivided into smaller visual areas, the spatial organization of neuronal responses to visual stimuli can be effectively measured and mapped using a task-based fMRI method that localizes visual areas in the occipital lobe via a block design paradigm or population receptive field mapping.[100] Retinotopic mapping is useful for characterizing damage to the visual cortex or pathways, as well as identifying plastic changes associated with reorganization. In one study, retinotopic maps revealed increased population receptive field values in a blindsighted patient, suggesting neural reorganization as the mechanism behind blindsight[99] (Fig. 9a–d). DTI and fMRI can provide anatomical and functional frameworks for blindsighted brains and can even reveal etiological differences in patients experiencing similar visual deficits[120,121] (Fig. 11). Of note, children with acquired hemianopia did not exhibit blindsight, as evidenced by their behavioral performance and BOLD activation patterns.[119] These findings may offer insight into the mechanisms of vision impairment and have potential implications in vision restoration.

Over the past few years, MRI has been used to test the efficacy of rehabilitation techniques for hemianopia by assessing neurological changes pre- and posttreatment. One study used both resting-state and task-based fMRI paradigms to detect increased activation in the right temporoparietal junction of the attentional functional network after visual rehabilitation training.[122] With a more homogeneous patient sample, fMRI can potentially be used to uncover mechanisms of recovery. Other rehabilitation techniques like neurostimulation also involve the use of pre- and post-fMRI to monitor neuronal changes elicited by interventions.[123] Posttraining fMRI after combined transcranial direct current stimulation and visual rehabilitation training revealed increased activation in perilesional regions in a patient with an occipital lesion, suggesting some recovery of visual function[124] (Fig. 10e).

Future Directions

MRI techniques can help reveal underlying changes in the visual cortex and higher-order visual areas associated with various vision disorders. These techniques can also uncover the mechanisms of visual plasticity resulting from rehabilitation therapy. In fact, the first CRISPR-Cas9 gene therapy study in humans used multiparametric MRI to demonstrate its long-term plasticity effects for vision restoration in Leber’s congenital amaurosis, the most common cause of inherited blindness in childhood. Utilizing DTI to examine microstructural integrity of the visual pathways and fMRI to evaluate visual cortical activation in patients receiving unilateral subretinal gene therapeutic injection versus sighted controls, MRI was able to elucidate the significant effects of both visual deprivation and restorative treatment on the visual system[125] (Fig. 12). Moving forward, the findings of MRI studies will need to be used more frequently alongside behavioral assessments to aid in clinical intervention.

CONCLUSION

In this review we detailed how MRI can be employed to examine visual system anatomy, physiology, pathology, and plasticity. Other noninvasive imaging modalities, such as ultrasound and optical coherence tomography, have proven invaluable in the clinical evaluation of certain visual disorders. However, their uses are largely limited to the

assessment of ocular and vascular etiologies, with optical coherence tomography requiring a clear visual axis within the ocular media. Visual field testing and intraocular pressure measurement are additional, key tools in routine clinical ophthalmologic assessments that can be conducted in a single outpatient ophthalmology visit. In contrast, computed tomography and MRI require referral, additional visits, image processing time, and a radiologist. Thus, these modalities must provide complementary, or more detailed, information than the above standard assessments to justify their inclusion in clinical practice. Whereas computed tomography is a vital diagnostic tool in neurologic imaging, MRI provides superior structural imaging of the soft tissues comprising the visual system, and is set apart from other techniques by specialized sequences that globally elucidate visual health and function.

As detailed in this review, MRI can provide a more comprehensive understanding of certain visual impairments, as well as potentially earlier diagnoses, compared to standard ophthalmologic assessments. Based on research over the last decade, we are only beginning to truly understand the full potential for MRI to change the way we examine the visual system. Diseases like glaucoma, once thought to be primarily ocular in nature, are now being shown to be more widespread and have observable functional and metabolic derangements in downstream brain structures, with some disturbances apparent before routine classification as glaucoma. Tools providing visualization of changes in the blood–ocular barrier, including contrast-enhanced imaging sequences demonstrating retinovascular function and ocular leakage in non-ocular diseases, are revealing important clues about complex pathophysiology and may allow for earlier detection and management of certain disorders. In visual restorative treatment ranging from visual perceptual learning to retinal gene therapy, MRI has been capable of assessing the long-term structural, metabolic, and functional aspects of visual system plasticity. Experimental techniques will likely continue providing new insights as clinical research advances.

Although MRI offers several advantages for ophthalmology in both clinical and translational research settings, there are still obstacles that need to be overcome, as detailed in the previous sections. While certain modalities, such as high-field structural MRI, fMRI, or metabolic MRS can help clinicians determine the cause or extent of disease, definitive diagnosis often still requires histopathologic examination. Contrast agents with toxicity concerns may require alternative routes of administration, chelation strategies, or other methods to minimize side effects while maximizing utility before they can be applied clinically. To improve image quality, specialized coil designs geared toward imaging particular anatomical regions may improve resolution for more accurate and detailed assessment. Novel image sequences can be optimized for specific pathologies to help clinicians diagnose and treat patients. Although the physiology that leads to normal and abnormal activity-dependent hemodynamic changes in fMRI still requires investigation, results from fMRI studies show that it can be key to uncovering the mechanisms of neuroplasticity and assessing the efficacy of future therapies in optic neuropathy and cortical vision loss. Through continued collaboration between the scientific and medical communities, we can devise new strategies to overcome these obstacles, expand our knowledge of the visual system, and improve quality of life in patients with vision loss.

ACKNOWLEDGMENT

We thank all the collaborators who contributed to the research articles upon which the present review is based.

Contract grant sponsor: National Institutes of Health; Contract grant number: R01-EY028125; Contract grant sponsor: BrightFocus Foundation; Contract grant numbers: G2013077, G2016030, and G2019103; Contract grant sponsor: Feldstein Medical Foundation; Contract grant sponsor: Research to Prevent Blindness/Stavros Niarchos Foundation International Research Collaborators Award; Contract grant sponsor: unrestricted grant from Research to Prevent Blindness to NYU Langone Health Department of Ophthalmology.

References

1. Pike MG, Holmstrom G, de Vries LS, et al. Patterns of visual impairment associated with lesions of the preterm infant brain. Dev Med Child Neurol 1994;36(10):849–862. [PubMed: 7926317]
2. Pineles SL, Demer JL. Bilateral abnormalities of optic nerve size and eye shape in unilateral amblyopia. Am J Ophthalmol 2009;148(4):551–557. [PubMed: 19573859]
3. Faiq MA, Wollstein G, Schuman JS, Chan KC. Cholinergic nervous system and glaucoma: From basic science to clinical applications. Prog Retin Eye Res 2019;72:100767. [PubMed: 31242454]
4. Gala F Magnetic resonance imaging of optic nerve. Indian J Radiol Imaging 2015;25(4):421–438. [PubMed: 26752822]
5. Hofer S, Karaus A, Frahm J. Reconstruction and dissection of the entire human visual pathway using diffusion tensor MRI. Front Neuroanat 2010;4:15. [PubMed: 20428499]
6. Vinogradov E, Degenhardt A, Smith D, et al. High-resolution anatomic, diffusion tensor, and magnetization transfer magnetic resonance imaging of the optic chiasm at 3T. J Magn Reson Imaging 2005;22(2):302–306. [PubMed: 16028247]
7. Grover VP, Tognarelli JM, Crossey MM, Cox IJ, Taylor-Robinson SD, McPhail MJ. Magnetic resonance imaging: Principles and techniques: Lessons for clinicians. J Clin Exp Hepatol 2015;5(3):246–255. [PubMed: 26628842]
8. Hoff MN, AT MK, Shellock FG, et al. Safety considerations of 7-T MRI in clinical practice. Radiology 2019;292(3):509–518. [PubMed: 31310177]
9. Ladd ME, Bachert P, Meyerspeer M, et al. Pros and cons of ultra-high-field MRI/MRS for human application. Prog Nucl Magn Reson Spectrosc 2018;109:1–50. [PubMed: 30527132]
10. Krupa K, Bekiesinska-Figatowska M. Artifacts in magnetic resonance imaging. Pol J Radiol 2015;80:93–106. [PubMed: 25745524]
11. Sati P, George IC, Shea CD, Gaitan MI, Reich DS. FLAIR*: A combined MR contrast technique for visualizing white matter lesions and parenchymal veins. Radiology 2012;265(3):926–932. [PubMed: 23074257]
12. Eide PK, Ringstad G. Delayed clearance of cerebrospinal fluid tracer from entorhinal cortex in idiopathic normal pressure hydrocephalus: A glymphatic magnetic resonance imaging study. J Cereb Blood Flow Metab 2019;39(7):1355–1368. [PubMed: 29485341]
13. Ringstad G, Vatnehol SAS, Eide PK. Glymphatic MRI in idiopathic normal pressure hydrocephalus. Brain 2017;140(10):2691–2705. [PubMed: 28969373]
14. Deng W, Liu C, Parra C, et al. Quantitative imaging of the clearance systems in the eye and the brain. Quant Imaging Med Surg 2020;10(1):1–14. [PubMed: 31956524]
15. Deng W, Faiq MA, Liu C, Adi V, Chan KC. Applications of manganese-enhanced magnetic resonance imaging in ophthalmology and visual neuroscience. Front Neural Circuits 2019;13:35. [PubMed: 31156399]
16. Huisman TA. Diffusion-weighted and diffusion tensor imaging of the brain, made easy. Cancer Imaging 2010;10:S163–S171. [PubMed: 20880787]
17. Thomason ME, Thompson PM. Diffusion imaging, white matter, and psychopathology. Annu Rev Clin Psychol 2011;7:63–85. [PubMed: 21219189]
18. Chen JE, Glover GH. Functional magnetic resonance imaging methods. Neuropsychol Rev 2015;25(3):289–313. [PubMed: 26248581]

19. Lee MH, Smyser CD, Shimony JS. Resting-state fMRI: A review of methods and clinical applications. AJNR Am J Neuroradiol 2013;34(10):1866–1872. [PubMed: 22936095]
20. Glover GH. Overview of functional magnetic resonance imaging. Neurosurg Clin N Am 2011;22(2):133–139. [PubMed: 21435566]
21. Nishihara H, Nakasato M, Sawa H, et al. A case of central nervous system lymphomatoid granulomatosis; characteristics of PET imaging and pathological findings. J Neurooncol 2009;93(2):275–278. [PubMed: 19104755]
22. Bekerman I, Gottlieb P, Vaiman M. Variations in eyeball diameters of the healthy adults. J Ophthalmol 2014;2014:503645. [PubMed: 25431659]
23. Igbinedion BO, Ogbeide OU. Measurement of normal ocular volume by the use of computed tomography. Niger J Clin Pract 2013;16(3):315–319. [PubMed: 23771452]
24. Alamouti B, Funk J. Retinal thickness decreases with age: An OCT study. Br J Ophthalmol 2003;87(7):899–901. [PubMed: 12812895]
25. Lukats O, Vizkelety T, Markella Z, et al. Measurement of orbital volume after enucleation and orbital implantation. PLoS One 2012;7(12):e50333. [PubMed: 23236368]
26. Georgouli T, James T, Tanner S, et al. High-resolution microscopy coil MR-eye. Eye 2008;22(8):994–996. [PubMed: 17332767]
27. Beenakker JW, van Rijn GA, Luyten GP, Webb AG. High-resolution MRI of uveal melanoma using a microcoil phased array at 7T. NMR Biomed 2013;26(12):1864–1869. [PubMed: 24123279]
28. Ferreira TA, Saraiva P, Genders SW, Buchem MV, Luyten GPM, Beenakker JW. CT and MR imaging of orbital inflammation. Neuroradiology 2018;60(12):1253–1266. [PubMed: 30310941]
29. Lacheta D, Miskiewicz P, Gluszko A, et al. Immunological aspects of Graves' ophthalmopathy. Biomed Res Int 2019;2019:7453260. [PubMed: 31781640]
30. Mayer EJ, Fox DL, Herdman G, et al. Signal intensity, clinical activity and cross-sectional areas on MRI scans in thyroid eye disease. Eur J Radiol 2005;56(1):20–24. [PubMed: 15896938]
31. Daumerie C, Duprez T, Boschi A. Long-term multidisciplinary follow-up of unilateral thyroid-associated orbitopathy. Eur J Intern Med 2008;19(7):531–536. [PubMed: 19013383]
32. Ferreira TA, Grech Fonk L, Jaarsma-Coes MG, van Haren GGR, Marinkovic M, Beenakker JM. MRI of uveal melanoma. Cancers 2019;11(3):377–396.
33. Beenakker JW, Ferreira TA, Soemarwoto KP, et al. Clinical evaluation of ultra-high-field MRI for three-dimensional visualisation of tumour size in uveal melanoma patients, with direct relevance to treatment planning. Magma 2016;29(3):571–577. [PubMed: 26915081]
34. Da M, Li KK, Chan KC, Wu EX, Wong DS. Distribution of triamcinolone acetonide after intravitreal injection into silicone oil-filled eye. Biomed Res Int 2016;2016:5485467. [PubMed: 27493959]
35. Jaarsma-Coes MG, Goncalves Ferreira TA, van Haren GR, Marinkovic M. Beenakker JM. MRI enables accurate diagnosis and follow-up in uveal melanoma patients after vitrectomy. Melanoma Res 2019;29(6):655–659. [PubMed: 30664105]
36. de Jong MC, de Graaf P, Pouwels PJW, et al. 9.4T and 17.6T MRI of retinoblastoma: ex vivo evaluation of microstructural anatomy and disease extent compared with histopathology. J Magn Reson Imaging 2018;47(6):1487–1497. [PubMed: 29193569]
37. Occhiutto ML, Freitas FR, Maranhao RC, Costa VP. Breakdown of the blood-ocular barrier as a strategy for the systemic use of nanosystems. Pharmaceutics 2012;4(2):252–275. [PubMed: 24300231]
38. Hitomi E, Simpkins AN, Luby M, Latour LL, Leigh RJ, Leigh R. Blood-ocular barrier disruption in patients with acute stroke. Neurology 2018;90(11):e915–e923. [PubMed: 29438039]
39. Forster A, Bohme J, Groden C, Wenz H. Gadolinium leakage in ocular structures in optic neuritis. J Clin Neurosci 2019;68:268–270. [PubMed: 31204221]
40. Trick GL, Edwards PA, Desai U, Morton PE, Latif Z, Berkowitz BA. MRI retinovascular studies in humans: Research in patients with diabetes. NMR Biomed 2008;21(9):1003–1012. [PubMed: 18821575]

41. Ho LC, Sigal IA, Jan NJ, et al. Non-invasive MRI assessments of tissue microstructures and macromolecules in the eye upon biomechanical or biochemical modulation. Sci Rep 2016;6:32080. [PubMed: 27561353]
42. Ho LC, Sigal IA, Jan NJ, et al. Magic angle-enhanced MRI of fibrous microstructures in sclera and cornea with and without intraocular pressure loading. Invest Ophthalmol Vis Sci 2014;55(9):5662–5672. [PubMed: 25103267]
43. Beenakker JM, Wezel J, Groen J, Webb AG, Bornert P. Silent volumetric multi-contrast 7 Tesla MRI of ocular tumors using zero Echo time imaging. PLoS One 2019;14(9):e0222573. [PubMed: 31525248]
44. Berkowitz BA. Oxidative stress measured in vivo without an exogenous contrast agent using QUEST MRI. J Magn Reson 2018;291:94–100. [PubMed: 29705036]
45. Hoch MJ, Bruno MT, Shepherd TM. Advanced MRI of the optic nerve. J Neuroophthalmol 2017;37(2):187–196. [PubMed: 28459736]
46. Minalga E, Rose J, Choi SE, et al. A 20-channel coil for improved magnetic resonance imaging of the optic nerve. Concepts Magn Reson B 2011;39B(1):26–36.
47. Kim HJ, Paul F, Lana-Peixoto MA, et al. MRI characteristics of neuromyelitis optica spectrum disorder: An international update. Neurology 2015;84(11):1165–1173. [PubMed: 25695963]
48. Wan H, He H, Zhang F, Sha Y, Tian G. Diffusion-weighted imaging helps differentiate multiple sclerosis and neuromyelitis optica-related acute optic neuritis. J Magn Reson Imaging 2017;45(6):1780–1785. [PubMed: 27859858]
49. You Y, Joseph C, Wang C, et al. Demyelination precedes axonal loss in the transneuronal spread of human neurodegenerative disease. Brain 2019;142(2):426–442. [PubMed: 30668642]
50. Miller N, Liu Y, Krivochenitser R, Rokers B. Linking neural and clinical measures of glaucoma with diffusion magnetic resonance imaging (dMRI). PLoS One 2019;14(5):e0217011. [PubMed: 31150402]
51. Kim JW, Andersson JL, Seifert AC, et al. Incorporating non-linear alignment and multi-compartmental modeling for improved human optic nerve diffusion imaging. Neuroimage 2019;196:102–113. [PubMed: 30930313]
52. Mascioli G, Salvolini S, Cavola GL, et al. Functional MRI examination of visual pathways in patients with unilateral optic neuritis. Radiol Res Pract 2012;2012:265306. [PubMed: 22852082]
53. Li J, Shi W, Li M, et al. Time-dependent diffusion tensor changes of optic nerve in patients with indirect traumatic optic neuropathy. Acta Radiol 2014;55(7):855–863. [PubMed: 24097827]
54. Yang QT, Fan YP, Zou Y, et al. Evaluation of traumatic optic neuropathy in patients with optic canal fracture using diffusion tensor magnetic resonance imaging: A preliminary report. ORL J Otorhinolaryngol Relat Spec 2011;73(6):301–307. [PubMed: 21952108]
55. De Paulis D, Nicosia G, Taddei G, et al. Intracranial aneurysms and optic glioma—An unusual combination: A case report. J Med Case Reports 2016;10:78.
56. Ryu WHA, Starreveld Y, Burton JM, Liu J, Costello F, Group PS. The utility of magnetic resonance imaging in assessing patients with pituitary tumors compressing the anterior visual pathway. J Neuroophthalmol 2017;37(3):230–238. [PubMed: 27391942]
57. Sengupta S, Smith DS, Smith AK, Welch EB, Smith SA. Dynamic imaging of the eye, optic nerve, and extraocular muscles with golden angle radial MRI. Invest Ophthalmol Vis Sci 2017;58(10):4390–4398. [PubMed: 28813574]
58. Alexander AL, Lee JE, Lazar M, Field AS. Diffusion tensor imaging of the brain. Neurotherapeutics 2007;4(3):316–329. [PubMed: 17599699]
59. Zhang Y, Guo X, Wang M, et al. Reduced field-of-view diffusion tensor imaging of the optic nerve in retinitis pigmentosa at 3T. AJNR Am J Neuroradiol 2016;37(8):1510–1515. [PubMed: 27056427]
60. Sun Z, Parra C, Bang JW, Fieremans E, Wollstein G, Schuman JS, Chan KC. Diffusion kurtosis imaging reveals optic tract damage that correlates with clinical severity in glaucoma. Conf Proc IEEE Eng Med Biol Soc. 2020;1746–1749.
61. Murphy MC, Nau AC, Fisher C, Kim SG, Schuman JS, Chan KC. Top-down influence on the visual cortex of the blind during sensory substitution. Neuroimage 2016;125:932–940. [PubMed: 26584776]

62. Aldusary N, Michels L, Traber GL, et al. Lateral geniculate nucleus volumetry at 3T and 7T: Four different optimized magnetic-resonance-imaging sequences evaluated against a 7T reference acquisition. Neuroimage 2019;186:399–409. [PubMed: 30342237]
63. Kasi A, Faiq MA, Chan KC. In vivo imaging of structural, metabolic and functional brain changes in glaucoma. Neural Regen Res 2019;14(3):446–449. [PubMed: 30539811]
64. Trivedi V, Bang JW, Parra C, et al. Widespread brain reorganization perturbs visuomotor coordination in early glaucoma. Sci Rep 2019;9(1):14168. [PubMed: 31578409]
65. Dai H, Mu KT, Qi JP, et al. Assessment of lateral geniculate nucleus atrophy with 3T MR imaging and correlation with clinical stage of glaucoma. AJNR Am J Neuroradiol 2011;32(7):1347–1353. [PubMed: 21757515]
66. Furlanetto RL, Teixeira SH, Gracitelli CPB, et al. Structural and functional analyses of the optic nerve and lateral geniculate nucleus in glaucoma. PLoS One 2018;13(3):e0194038. [PubMed: 29570721]
67. Schmidt MA, Knott M, Heidemann R, et al. Investigation of lateral geniculate nucleus volume and diffusion tensor imaging in patients with normal tension glaucoma using 7 Tesla magnetic resonance imaging. PLoS One 2018;13(6):e0198830. [PubMed: 29879191]
68. Lee JY, Jeong HJ, Lee JH, et al. An investigation of lateral geniculate nucleus volume in patients with primary open-angle glaucoma using 7 Tesla magnetic resonance imaging. Invest Ophthalmol Vis Sci 2014; 55(6):3468–3476. [PubMed: 24722700]
69. Li M, Ke M, Song Y, Mu K, Zhang H, Chen Z. Diagnostic utility of central damage determination in glaucoma by magnetic resonance imaging: An observational study. Exp Ther Med 2019;17(3):1891–1895. [PubMed: 30783465]
70. Zhang P, Wen W, Sun X, He S. Selective reduction of fMRI responses to transient achromatic stimuli in the magnocellular layers of the LGN and the superficial layer of the SC of early glaucoma patients. Hum Brain Mapp 2016;37(2):558–569. [PubMed: 26526339]
71. Zhang Y, Chen X, Wen G, Wu G, Zhang X. Proton magnetic resonance spectroscopy ((1)H-MRS) reveals geniculocalcarine and striate area degeneration in primary glaucoma. PLoS One 2013;8(8):e73197. [PubMed: 24009739]
72. Doganay S, Cankaya C, Alkan A. Evaluation of corpus geniculatum laterale and vitreous fluid by magnetic resonance spectroscopy in patients with glaucoma; a preliminary study. Eye 2012;26(8):1044–1051. [PubMed: 22627479]
73. Aksoy DO, Umurhan Akkan JC, Alkan A, Aralasmak A, Otcu Temur H, Yurtsever I. Magnetic resonance spectroscopy features of the visual pathways in patients with glaucoma. Clin Neuroradiol 2019;29(4):615–621. [PubMed: 30291364]
74. Levi DM, Knill DC, Bavelier D. Stereopsis and amblyopia: A mini-review. Vision Res 2015;114:17–30. [PubMed: 25637854]
75. Levi DM, Li RW. Perceptual learning as a potential treatment for amblyopia: A mini-review. Vision Res 2009;49(21):2535–2549. [PubMed: 19250947]
76. Hess RF, Thompson B, Gole G, Mullen KT. Deficient responses from the lateral geniculate nucleus in humans with amblyopia. Eur J Neurosci 2009;29(5):1064–1070. [PubMed: 19291231]
77. Hess RF, Thompson B, Gole GA, Mullen KT. The amblyopic deficit and its relationship to geniculo-cortical processing streams. J Neurophysiol 2010;104(1):475–483. [PubMed: 20463193]
78. Coullon GS, Jiang F, Fine I, Watkins KE, Bridge H. Subcortical functional reorganization due to early blindness. J Neurophysiol 2015;113(7):2889–2899. [PubMed: 25673746]
79. Gupta S, Kumaran SS, Saxena R, Gudwani S, Menon V, Sharma P. BOLD fMRI and DTI in strabismic amblyopes following occlusion therapy. Int Ophthalmol 2016;36(4):557–568. [PubMed: 26659010]
80. Nooij RP, Hoving EW, van Hulzen AL, Cornelissen FW, Renken RJ. Preservation of the optic radiations based on comparative analysis of diffusion tensor imaging tractography and anatomical dissection. Front Neuroanat 2015;9:96. [PubMed: 26300739]
81. Li Q, Jiang Q, Guo M, Li Q, Cai C, Yin X. Grey and white matter changes in children with monocular amblyopia: Voxel-based morphometry and diffusion tensor imaging study. Br J Ophthalmol 2013; 97(4):524–529. [PubMed: 23343654]

82. de Blank PM, Berman JI, Liu GT, Roberts TP, Fisher MJ. Fractional anisotropy of the optic radiations is associated with visual acuity loss in optic pathway gliomas of neurofibromatosis type 1. Neuro Oncol 2013;15(8):1088–1095. [PubMed: 23658320]
83. Murphy MC, Conner IP, Teng CY, et al. Retinal structures and visual cortex activity are impaired prior to clinical vision loss in glaucoma. Sci Rep 2016;6:31464. [PubMed: 27510406]
84. Martinez-Heras E, Varriano F, Prckovska V, et al. Improved framework for tractography reconstruction of the optic radiation. PLoS One 2015;10(9):e0137064. [PubMed: 26376179]
85. Miller DH, Johnson G, Tofts PS, MacManus D, McDonald WI. Precise relaxation time measurements of normal-appearing white matter in inflammatory central nervous system disease. Magn Reson Med 1989;11(3):331–336. [PubMed: 2779420]
86. Bitsch A, Bruhn H, Vougioukas V, et al. Inflammatory CNS demyelination: Histopathologic correlation with in vivo quantitative proton MR spectroscopy. AJNR Am J Neuroradiol 1999;20(9):1619–1627. [PubMed: 10543631]
87. Zeng C, Du S, Han Y, et al. Optic radiations are thinner and show signs of iron deposition in patients with long-standing remitting-relapsing multiple sclerosis: An enhanced T2(*)-weighted angiography imaging study. Eur Radiol 2018;28(10):4447–4454. [PubMed: 29713769]
88. Wang C, Klistorner A, Ly L, Barnett MH. White matter tract-specific quantitative analysis in multiple sclerosis: Comparison of optic radiation reconstruction techniques. PLoS One 2018;13(1):e0191131. [PubMed: 29342192]
89. Reich DS, Smith SA, Gordon-Lipkin EM, et al. Damage to the optic radiation in multiple sclerosis is associated with retinal injury and visual disability. Arch Neurol 2009;66(8):998–1006. [PubMed: 19667222]
90. Allen B, Spiegel DP, Thompson B, Pestilli F, Rokers B. Altered white matter in early visual pathways of humans with amblyopia. Vision Res 2015;114:48–55. [PubMed: 25615840]
91. Xie S, Gong GL, Xiao JX, et al. Underdevelopment of optic radiation in children with amblyopia: A tractography study. Am J Ophthalmol 2007;143(4):642–646. [PubMed: 17276381]
92. Qi S, Mu YF, Cui LB, et al. Association of optic radiation integrity with cortical thickness in children with anisometropic amblyopia. Neurosci Bull 2016;32(1):51–60. [PubMed: 26769488]
93. Garaci FG, Bolacchi F, Cerulli A, et al. Optic nerve and optic radiation neurodegeneration in patients with glaucoma: in vivo analysis with 3-T diffusion-tensor MR imaging. Radiology 2009;252(2):496–501. [PubMed: 19435941]
94. Boucard CC, Hanekamp S, Curcic-Blake B, Ida M, Yoshida M, Cornelissen FW. Neurodegeneration beyond the primary visual pathways in a population with a high incidence of normal-pressure glaucoma. Ophthalmic Physiol Opt 2016;36(3):344–353. [PubMed: 27112227]
95. Sidek S, Ramli N, Rahmat K, Ramli NM, Abdulrahman F, Kuo TL. In vivo proton magnetic resonance spectroscopy (1H-MRS) evaluation of the metabolite concentration of optic radiation in primary open angle glaucoma. Eur Radiol 2016;26(12):4404–4412. [PubMed: 26943134]
96. Lim JC, Phal PM, Desmond PM, et al. Probabilistic MRI tractography of the optic radiation using constrained spherical deconvolution: A feasibility study. PLoS One 2015;10(3):e0118948. [PubMed: 25742640]
97. Winston GP, Daga P, White MJ, et al. Preventing visual field deficits from neurosurgery. Neurology 2014;83(7):604–611. [PubMed: 25015363]
98. Fischl B, Dale AM. Measuring the thickness of the human cerebral cortex from magnetic resonance images. Proc Natl Acad Sci U S A 2000;97(20):11050–11055. [PubMed: 10984517]
99. Georgy L, Jans B, Tamietto M, Ptito A. Functional reorganization of population receptive fields in a hemispherectomy patient with blindsight. Neuropsychologia 2019;128:198–203. [PubMed: 29969591]
100. Dumoulin SO, Knapen T. How visual cortical organization is altered by ophthalmologic and neurologic disorders. Annu Rev Vis Sci 2018;4:357–379. [PubMed: 29889657]
101. Wang TH, Jingami N, Okada T, Yunoki T, Ohtsuru S, Koike K. Anterior choroidal artery infarction evaluated with (123)I-imp single-photon emission computed tomography and 7 Tesla magnetic resonance imaging. J Stroke Cerebrovasc Dis 2019;28(5):e51–e52. [PubMed: 30862395]

102. Rutland JW, Delman BN, Huang KH, et al. Primary visual cortical thickness in correlation with visual field defects in patients with pituitary macroadenomas: A structural 7-Tesla retinotopic analysis. J Neurosurg 2019;1–11.
103. Ding K, Liu Y, Yan X, Lin X, Jiang T. Altered functional connectivity of the primary visual cortex in subjects with amblyopia. Neural Plast 2013;2013:612086. [PubMed: 23844297]
104. Watanabe T, Sasaki Y. Perceptual learning: Toward a comprehensive theory. Annu Rev Psychol 2015;66:197–221. [PubMed: 25251494]
105. Levi DM. Prentice Award Lecture 2011: Removing the brakes on plasticity in the amblyopic brain. Optom Vis Sci 2012;89(6):827–838. [PubMed: 22581119]
106. Polat U, Ma-Naim T, Belkin M, Sagi D. Improving vision in adult amblyopia by perceptual learning. Proc Natl Acad Sci U S A 2004;101(17):6692–6697. [PubMed: 15096608]
107. Zhou Y, Huang C, Xu P, et al. Perceptual learning improves contrast sensitivity and visual acuity in adults with anisometropic amblyopia. Vision Res 2006;46(5):739–750. [PubMed: 16153674]
108. Yotsumoto Y, Watanabe T, Sasaki Y. Different dynamics of performance and brain activation in the time course of perceptual learning. Neuron 2008;57(6):827–833. [PubMed: 18367084]
109. Yu Q, Zhang P, Qiu J, Fang F. Perceptual learning of contrast detection in the human lateral geniculate nucleus. Curr Biol 2016;26(23):3176–3182. [PubMed: 27839973]
110. Shibata K, Sasaki Y, Bang JW, et al. Overlearning hyperstabilizes a skill by rapidly making neurochemical processing inhibitory-dominant. Nat Neurosci 2017;20(3):470–475. [PubMed: 28135242]
111. Lewis CM, Baldassarre A, Committeri G, Romani GL, Corbetta M. Learning sculpts the spontaneous activity of the resting human brain. Proc Natl Acad Sci U S A 2009;106(41):17558–17563. [PubMed: 19805061]
112. Kang DW, Kim D, Chang LH, et al. Structural and functional connectivity changes beyond visual cortex in a later phase of visual perceptual learning. Sci Rep 2018;8(1):5186. [PubMed: 29581455]
113. Bridge H, Jindahra P, Barbur J, Plant GT. Imaging reveals optic tract degeneration in hemianopia. Invest Ophthalmol Vis Sci 2011;52(1):382–388. [PubMed: 20739474]
114. Haaga M, Trauzettel-Klosinski S, Krumm A, et al. Homonymous hemianopia in children and adolescents: An MRI study. Neuropediatrics 2018;49(2):142–149. [PubMed: 29351692]
115. Goodwin D Homonymous hemianopia: Challenges and solutions. Clin Ophthalmol 2014;8:1919–1927. [PubMed: 25284978]
116. Chokron S, Perez C, Obadia M, Gaudry I, Laloum L, Gout O. From blindsight to sight: Cognitive rehabilitation of visual field defects. Restor Neurol Neurosci 2008;26(4–5):305–320. [PubMed: 18997308]
117. Millington RS, Yasuda CL, Jindahra P, et al. Quantifying the pattern of optic tract degeneration in human hemianopia. J Neurol Neurosurg Psychiatry 2014;85(4):379–386. [PubMed: 24163431]
118. Perez C, Peyrin C, Cavezian C, et al. An FMRI investigation of the cortical network underlying detection and categorization abilities in hemianopic patients. Brain Topogr 2013;26(2):264–277. [PubMed: 22878845]
119. Tinelli F, Cicchini GM, Arrighi R, Tosetti M, Cioni G, Morrone MC. Blindsight in children with congenital and acquired cerebral lesions. Cortex 2013;49(6):1636–1647. [PubMed: 22939919]
120. Celeghin A, Diano M, de Gelder B, Weiskrantz L, Marzi CA, Tamietto M. Intact hemisphere and corpus callosum compensate for visuomotor functions after early visual cortex damage. Proc Natl Acad Sci U S A 2017;114(48):E10475–E10483. [PubMed: 29133428]
121. Martin MB, Santos-Lozano A, Martin-Hernandez J, et al. Cerebral versus ocular visual impairment: The impact on developmental neuroplasticity. Front Psychol 2016;7:1958. [PubMed: 28082927]
122. Lu Q, Wang X, Li L, et al. Visual rehabilitation training alters attentional networks in hemianopia: An fMRI study. Clin Neurophysiol 2018;129(9):1832–1841. [PubMed: 29981958]
123. Urbanski M, Coubard OA, Bourlon C. Visualizing the blind brain: Brain imaging of visual field defects from early recovery to rehabilitation techniques. Front Integr Neurosci 2014;8:74. [PubMed: 25324739]

124. Plow EB, Obretenova SN, Halko MA, et al. Combining visual rehabilitative training and noninvasive brain stimulation to enhance visual function in patients with hemianopia: A comparative case study. Pm R 2011;3(9):825–835. [PubMed: 21944300]

125. Ashtari M, Zhang H, Cook PA, et al. Plasticity of the human visual system after retinal gene therapy in patients with Leber's congenital amaurosis. Sci Transl Med 2015;7(296):296ra110.

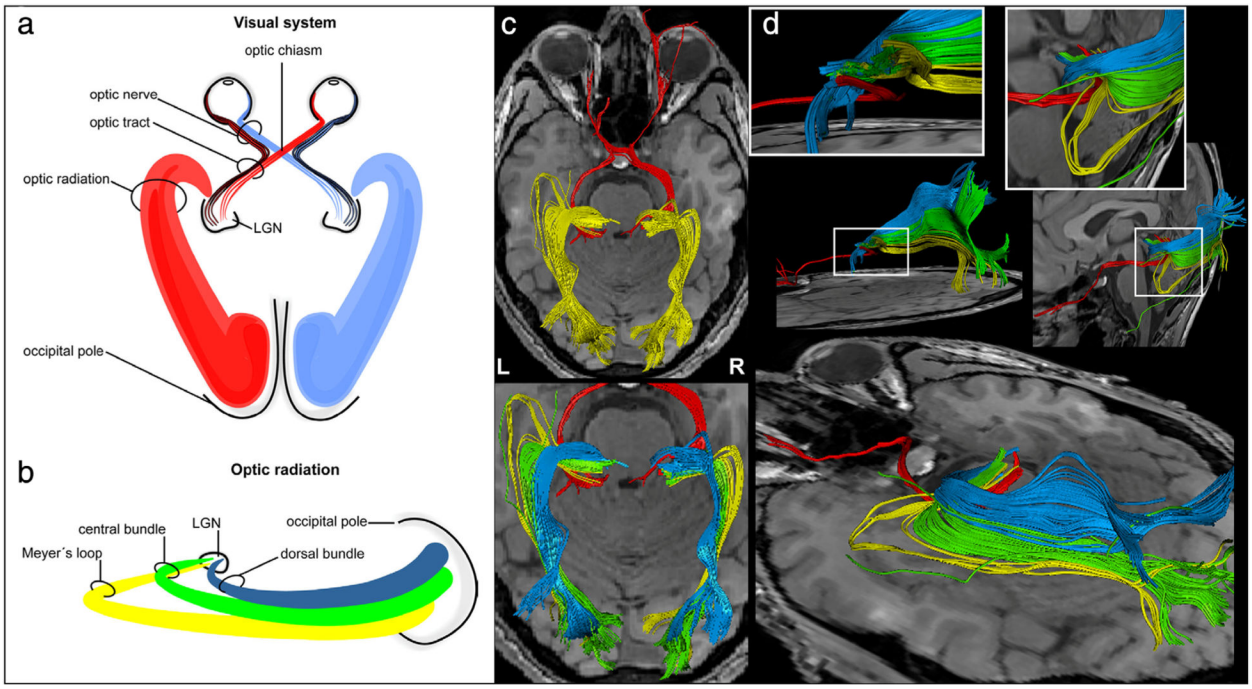

FIGURE 1:

Visual system anatomy. (a,b) Schematic representation of the entire visual pathway in axial view (a) and the optic radiations in sagittal view (b), extending from the lateral geniculate nucleus (LGN) to the cortex. (c,d) Diffusion tensor imaging (DTI) reconstructions of the visual pathway in successive axial planes (c) and in the sagittal plane (d), with emphasis on the spatial relationship of the three bundles of the optic radiations. Adapted with permission from Ref. 5.

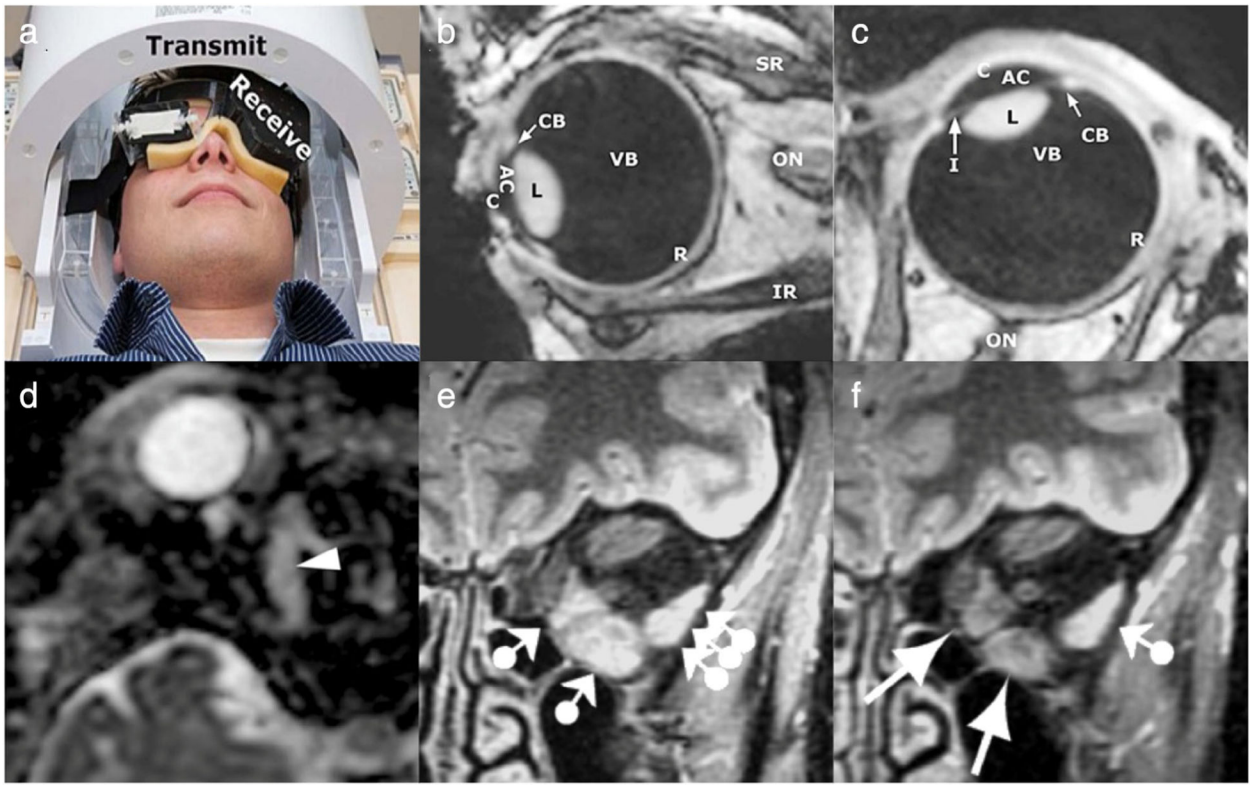

FIGURE 2:

Structural imaging of normal ocular anatomy and orbital pathology. (a–c) High-resolution structural MRI of the eye and orbit using a microcoil array. A three-channel receive eye microcoil array was developed and integrated alongside a transmit quadrature head coil (a) for in vivo 7T imaging. Using an intermittent blinking paradigm with a 3D inversion recovery turbo gradient echo imaging technique, sagittal (b) and transverse (c) images of the eye and nearby tissue were acquired in a healthy volunteer. AC = anterior chamber; C = cornea; CB = ciliary body; I = iris; IR = inferior rectus; L = lens; ON = optic nerve; R = retina and sclera; SR = superior rectus; VB = vitreous body. (d) Inflammatory myositis of the right superior oblique muscle, as visualized here on axial apparent diffusion coefficient (ADC) via diffusion-weighted MRI using an echo planar imaging sequence. No diffusion restriction is observed along the superior oblique muscle (arrowhead), and additional enhanced T_1-weighted images with fat signal suppression (not depicted) demonstrated enlargement and contrast enhancement of the muscle with surrounding cellulitis, all of which favor inflammation over infection or malignancy. Patient improved after corticosteroids and avoided biopsy. (e,f) Longitudinal imaging of a patient with thyroid eye disease, using frontal short tau inversion-recovery (STIR) images with 4-mm slice thickness. Initial MRI workup (e) occurred 12 months after disease onset in the left eye. Normal signal intensity was observed in all right eye extraocular muscles (not depicted) and the left superior rectus and superior oblique muscles, indicating lack of acute inflammation. The left medial and inferior rectus muscles displayed increased signal intensity as well as enlargement, indicating active inflammation (ball-arrowheads). The lateral rectus muscle, despite appearing normal in size on T_1-weighted spin echo imaging (not depicted), was

also found to have increased signal representing active disease (triple ball-arrowheads). At 7-year follow-up (f), the signal was unchanged in the left superior rectus and superior oblique muscles, and increased signal intensity of the lateral rectus muscle remained, likely indicating active inflammation in chronic thyroid eye disease (ball-arrowhead). Signal intensity of the left medial and inferior rectus muscle normalized (arrows), with decreased size noted on T_1-weighted spin-echo imaging, suggesting decreased disease activity in these muscles. Adapted with permissions from Refs. 27, 28, 31.

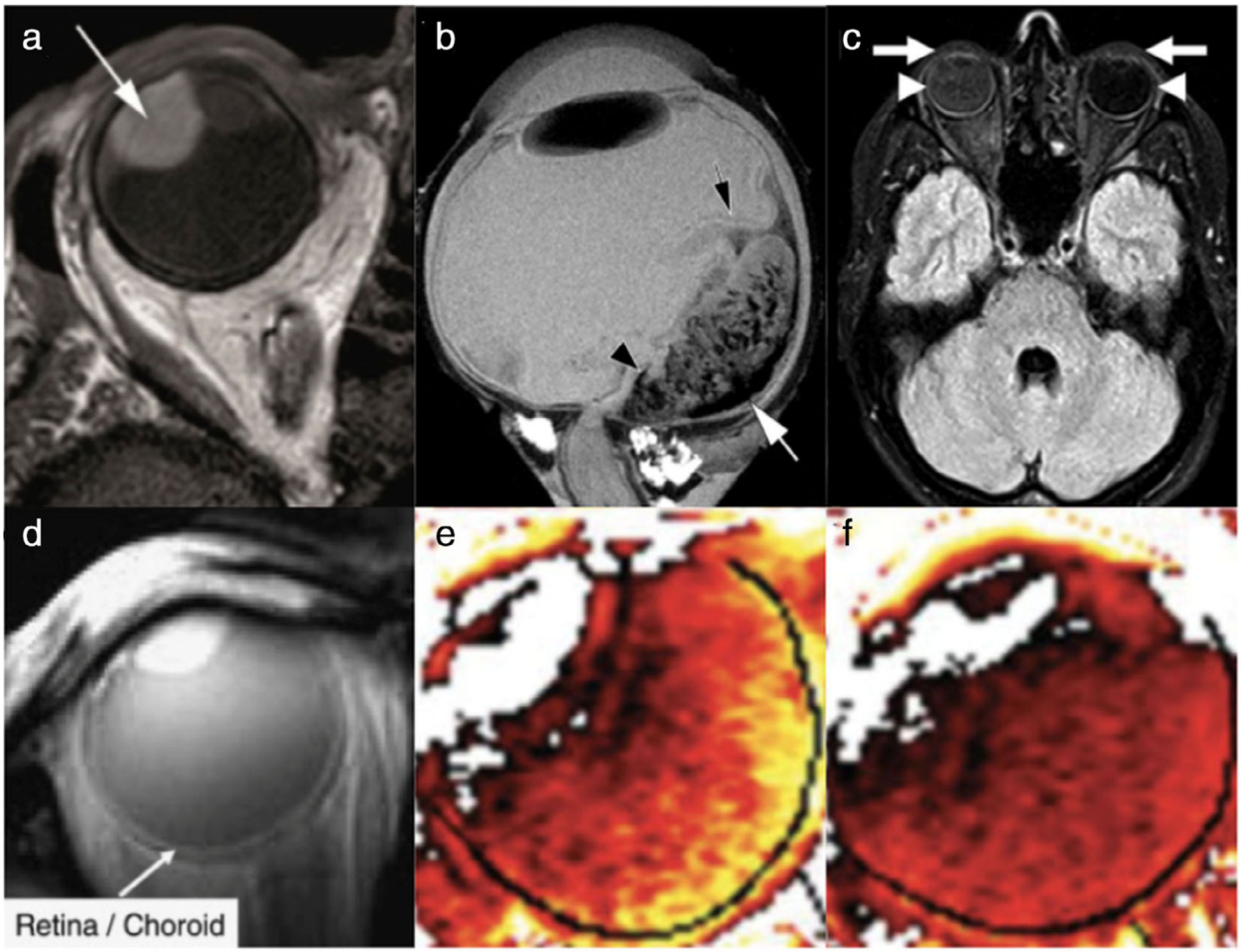

FIGURE 3:

Intraocular tumors and blood–ocular barrier physiology. (a) Uveal melanoma (arrow) in the right eye of a patient, shown here on axial multislice 2-mm T_1-weighted imaging at 3T. (b) Exophytic retinoblastoma imaged ex vivo using T_2-weighted rapid acquisition with relaxation enhancement (RARE) sequence at 9.4T following enucleation of the eye. The black arrow denotes a partial retinal detachment, which was a consequence of this tumor. The white arrow indicates potential hemosiderin deposition, and the black arrowhead marks a hypointense area found to correspond to hemorrhage via further histopathology. (c) Gadolinium leakage into ocular structures (GLOS) in a patient with right optic neuritis, on axial fluid-attenuated inversion recovery (FLAIR) sequence 1.5T MRI; the patient's right side is on the left side of this image. In this patient, GLOS was bilateral but asymmetric, observed more prominently ipsilateral to the unilateral optic neuritis. GLOS can be seen in the anterior chamber (arrows) and vitreous body (arrowheads). (d–f) MRI evaluation of blood–retinal barrier damage (d) and retinal oxygenation response (ROR) (e,f). Dynamic contrast-enhanced MRI (DCE-MRI) had an in-plane resolution of 390 μm^2 (12-mm slice thickness), as seen on this coronal image (d) illustrating the retina/choroid complex (ie, white line along the posterior aspect of the eye). The ROR in the preretinal vitreous was studied by taking advantage of the paramagnetic oxygen contrast in direct proportion to the change in oxygen concentration in the preretinal vitreous. Type I diabetic patients and

similar-age normal volunteers initially inhaled room air and then were switched to 100% O_2 for 40 minutes. MRI of the partial oxygen pressure (ΔPO_2) at 40 minutes demonstrates increased signal intensity in the preretinal vitreous of a diabetic patient with no retinopathy (e) compared to a control volunteer (f) of the same age. Lighter color (yellow) corresponds to a higher ΔPO_2 (up to 250 mm Hg), and darker color (red) corresponds to a lower value. Adapted with permissions from Refs. 32, 36, 39, 40.

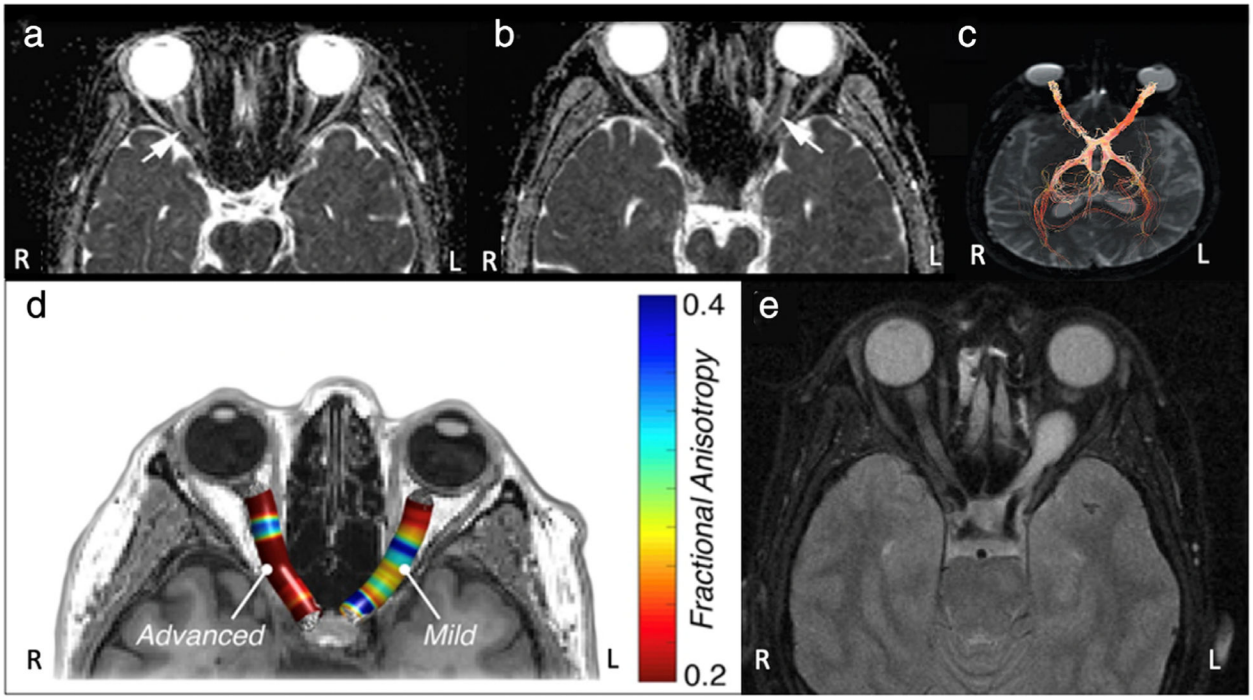

FIGURE 4:

MRI of the optic nerve. (a,b) Apparent diffusion coefficient (ADC) maps of a patient with multiple sclerosis-optic neuritis of the right optic nerve (a) and a patient with AQP4-IgG positive neuromyelitis optica-optic neuritis of the left optic nerve (b). Mean group ADC in the study was significantly lower in neuromyelitis optica-optic neuritis than in multiple sclerosis-optic neuritis. (c) Visual pathway fiber bundle tracking showing significantly lower nerve fiber bundle density in the optic nerve affected by indirect traumatic optic neuropathy (right) than in the normal nerve (left). (d) Fractional anisotropy (FA) map demonstrating significantly lower FA values in an optic nerve affected by advanced glaucoma (right) compared to the optic nerve with mild glaucoma (left). (e) Preoperative T_1-weighted MRI showing a left optic glioma. Adapted with permissions from Refs. 48, 50, 54, 55.

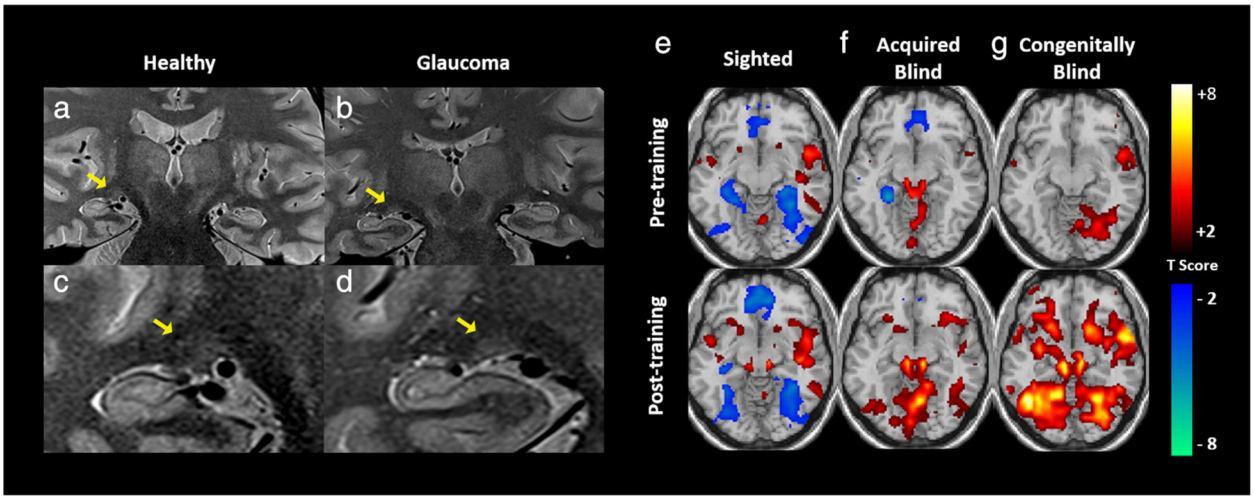

FIGURE 5:

Structural and functional MRI of the visual brain nuclei. (a–d) Structural MRI indicating atrophy of the lateral geniculate nucleus (LGN) in a glaucoma patient (b,d) in comparison with a healthy subject (a,c). (e–g) Functional MRI demonstrating activation maps before (top row) and after (bottom row) task training for interpretation of cross-modal visual information inputted via auditory stimulation in three study cohorts: sighted (e), acquired blind (f), and congenitally blind (g) individuals. As compared to sighted individuals, those with acquired or congenital blindness demonstrated increased activity in the subcortical nuclei, suggesting cross-modal sensory input is processed at this level in a distinct manner in this population. Adapted with permissions from Refs. 61, 66.

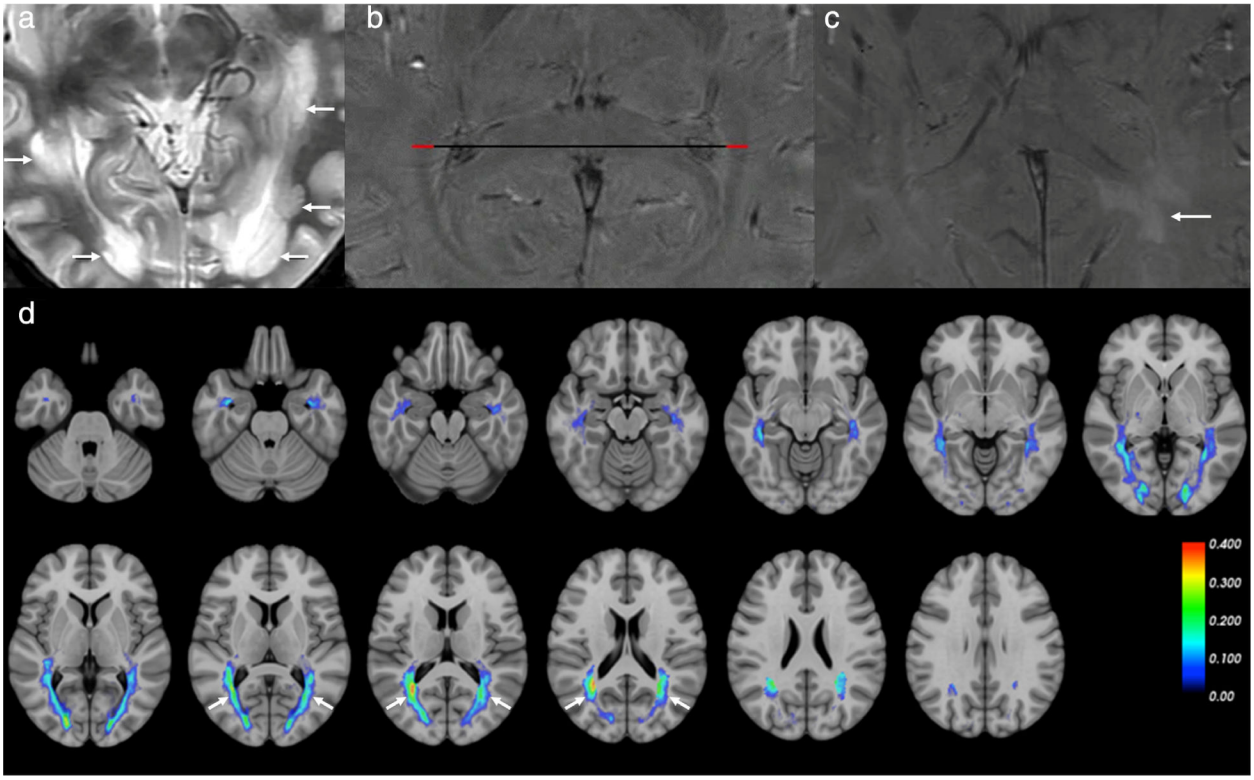

FIGURE 6:

MRI of the optic radiation in multiple sclerosis. (a) Conventional T_2-weighted imaging showed hyperintense signals of lesions in the optic radiation (arrows) in a multiple sclerosis patient. (b,c) Magnitude images of enhanced T_2*-weighted angiography imaging (ESWAN) showed symmetrical and hypointense signals within the optic radiation bilaterally in a healthy subject (b), while in a multiple sclerosis patient (c), the left optic radiation had more lesions (arrow). Red lines indicate the thickness of the optic radiations. (d) Optic radiation segmentation using the diffusion-based tractography approach showed that lesions were more frequent in the middle part of the optic radiation (arrows) adjacent to the lateral ventricle, compared with the anterior and posterior parts of the optic radiation. Adapted with permissions from Refs. 87, 88.

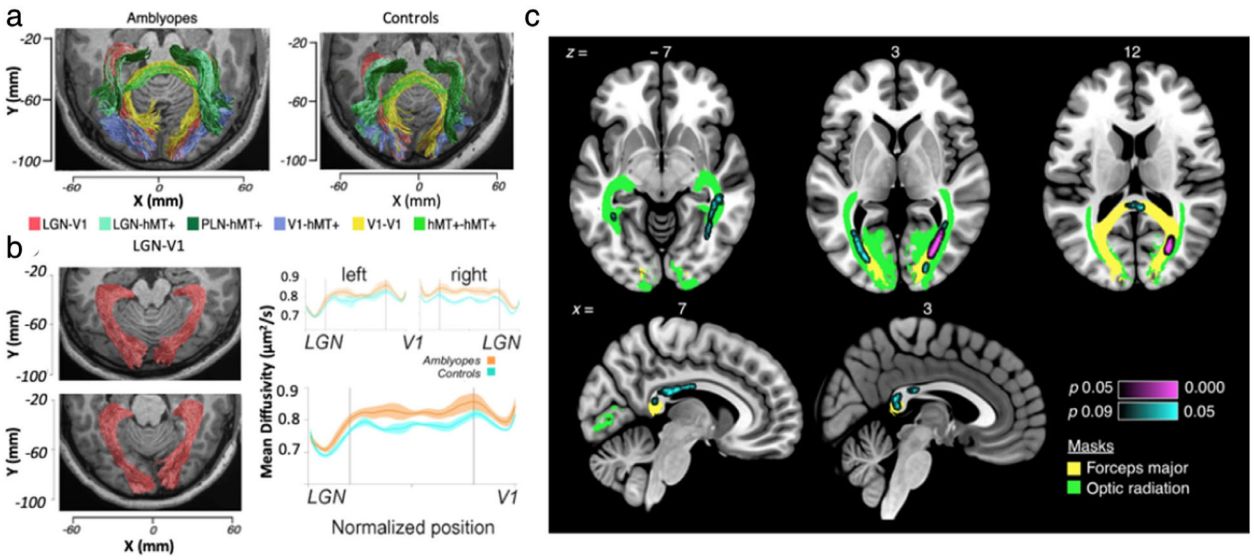

FIGURE 7:

Diffusion tensor imaging of the optic radiation in ophthalmic diseases. (a,b) Diffusion tensor imaging in amblyopia. Visual white matter pathways estimated by probabilistic tractography (a) in representative amblyopia (left) and control (right) participants. Pathways are color-coded. LGN-V1 (ie, the optic radiation) is red. LGN = lateral geniculate nucleus; V1 = primary visual cortex; V5/hMT + = human middle temporal visual cortex; PLN = pulvinar nucleus. (b) Visualized optic radiation pathway anatomy estimates in representative control (top left) and amblyopic (bottom left) participants, showing significantly increased mean diffusivity in amblyopes compared to controls (right). (c) Tract-based spatial statistics (TBSS) analysis revealed differences in fractional anisotropy (FA) in the white matter of glaucoma patients and controls. A significant difference in FA was found in a 380-voxel white matter region in three axial slices and two sagittal slices, using threshold-free cluster enhancement correction for multiple comparisons. Violet ($P < 0.05$) and cyan ($P < 0.09$) labeling show areas of decreased FA in glaucoma patients compared to controls. Green color labels the optic radiation, and yellow color labels the forceps major. Adapted with permissions from Refs. 90, 94.

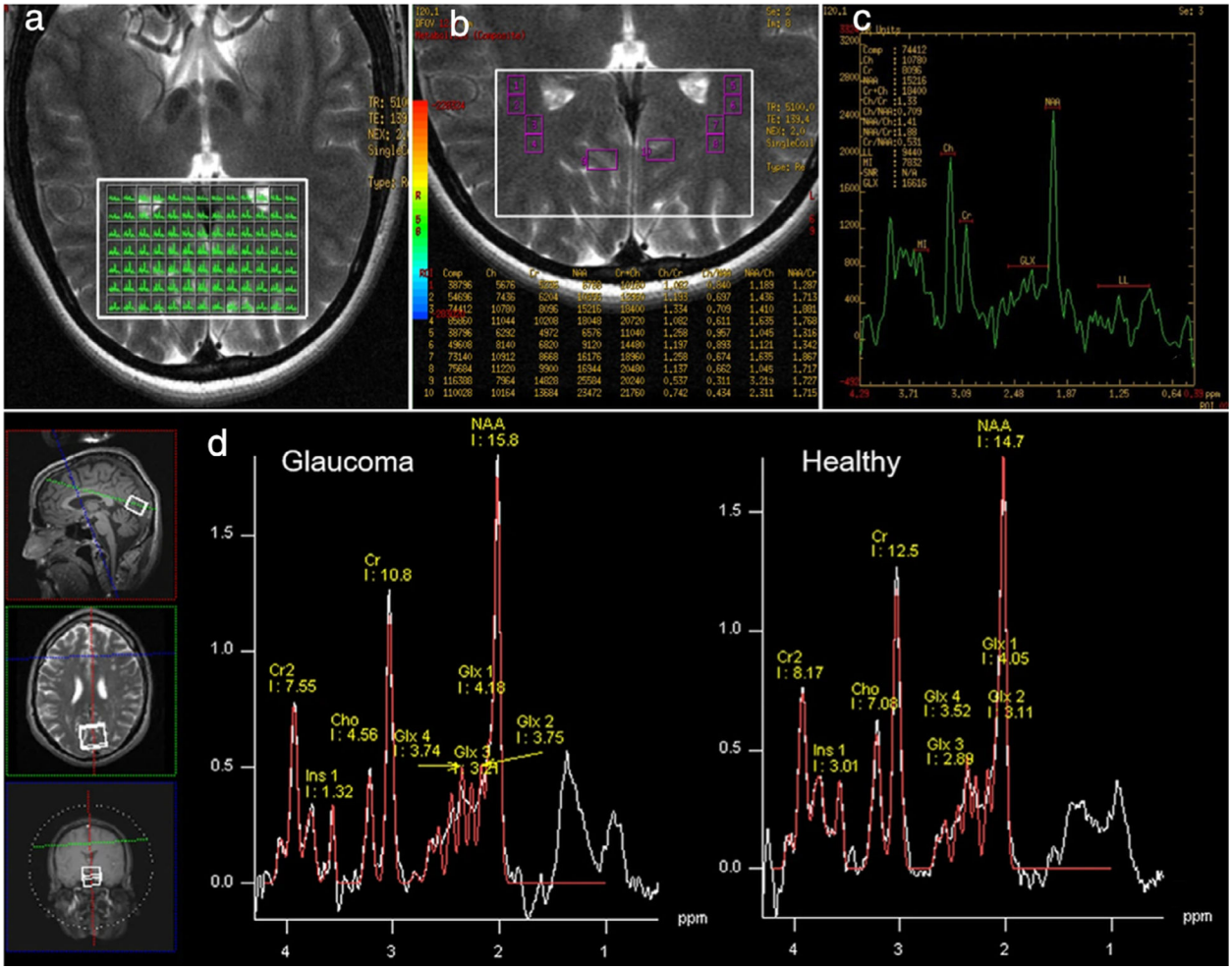

FIGURE 8:

Metabolic imaging of the optic radiation and visual cortex in glaucoma. (a–c) Multivoxel proton MRS. (a) displays all fixed-voxels in the volume of interest (VOI) (white box). The size of each voxel was 31.6 mm^2. (b) The amplification of (a). Several voxels were selected as regions of interest (ROIs) in the geniculocalcarine tracts (GCTs) and the striate area. ROI 1 through ROI 8 were distributed symmetrically on the GCTs. ROI 9 and ROI 10 were located in the striate area, each containing six voxels. (c) The spectrum of ROI 2 in the right GCT, with N-acetyl-aspartate (NAA) and choline (Cho) peaks. (d) Single-voxel proton MRS, where each proton MR spectrum was acquired using a 20 × 25 × 30 mm^3 voxel centered at the calcarine sulcus bilaterally, as shown in the anatomical images in three orthogonal planes (white boxes in left insets). Voxels covered both upper and lower visual field representations in each hemisphere. Here, we see sample proton MR spectrum (white curve) and fitted spectrum (red curve) of metabolic profiles in the primary visual cortex of a glaucoma patient (left) and a healthy subject (right). The levels of Cho, NAA, glutamate–glutamine complex (Glx), and creatine (Cr) brain metabolite contents were estimated from the spectrum. For quantitative comparisons, they were normalized to the Cr level. Adapted with permissions from Refs. 71, 83.

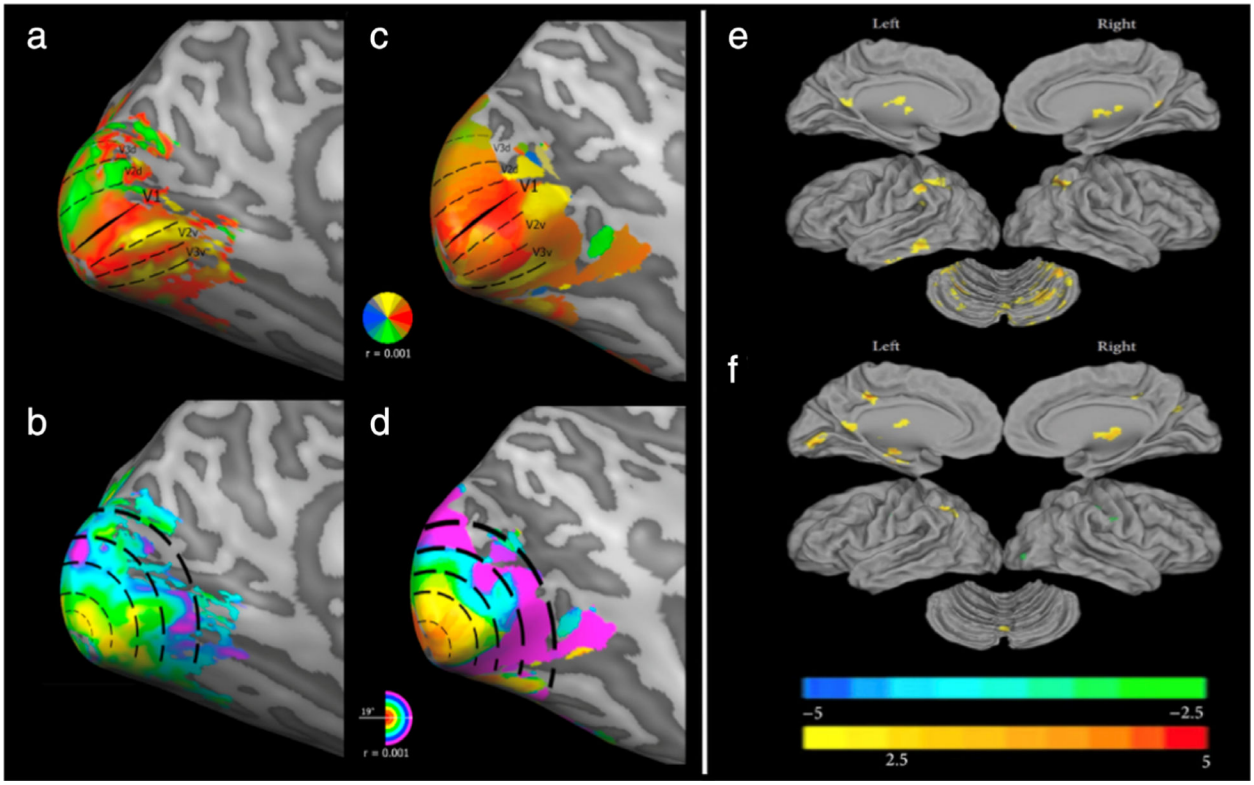

FIGURE 9:

Retinotopic mapping and cortical functional connectivity. (a–d) Retinotopic mapping. Retinotopic maps of a representative healthy control (a,b) vs. a patient with blindsight following a right functional hemispherectomy (c,d). Polar angle maps (a,c) show delineated visual areas V1, V2d, V3d, V2v, V3v in the left hemisphere. The dorsal visual areas above the calcarine sulcus and ending in “d” correspond to the contralateral (right) lower visual field quadrant, and the ventral visual areas ending in “v” correspond to the right upper visual field quadrant. Aside from the less clearly defined dorsal components (ie, blurred border between V2d and V3d), the retinotopic organization of the patient’s intact left visual areas did not differ substantially from those of healthy controls. Eccentricity maps (b,d) expectedly show a smooth and continuous phase progression of foveal representation in the occipital pole and peripheral representation in increasingly anterior locations. Compared to healthy controls, the patient with blindsight had a marked increase in population receptive field (pRF) sizes at 4–6° of eccentricity, with a size difference that reached ~300% between 8° and 10° (not depicted). Receptive field sizes at foveal and parafoveal eccentricities (≤4°) were not measurably altered. (e,f) Functional connectivity in amblyopia. Using resting-state fMRI, the anatomical distribution of functional connectivity alterations in mixed amblyopic (ie, anisometropic and strabismic) subjects is shown in comparison with normal sighted controls. Functional connectivity with the left primary visual cortex (V1; e) and right V1 (f), is individually visualized ($P < 0.01$, 130 voxels, AlphaSim corrected $p_{alpha} = 0.01$). Adapted with permissions from Refs. 99, 103.

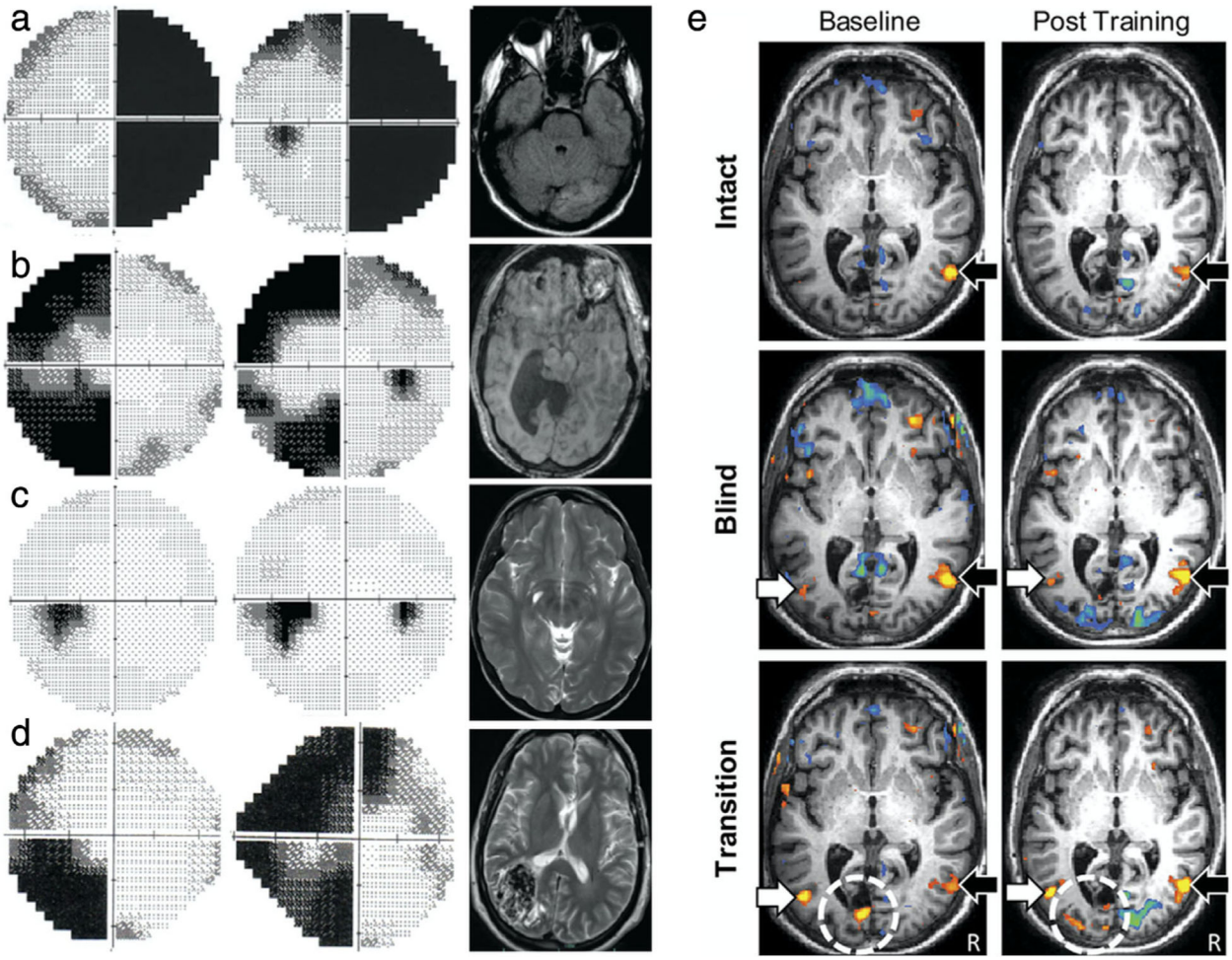

FIGURE 10:

Clinical MRI correlates in hemianopia and functional imaging of plasticity. (a–d) Examples of homonymous hemianopia with corresponding neuroimaging. (a) Axial T_1-weighted MRI with contrast in complete right homonymous hemianopia following a left occipital lobe stroke (right) affects the entire hemifield of both eyes (left). (b) Axial T_1-weighted MRI of left incongruous homonymous hemianopia with macular sparing due to hydrocephalus and subsequent shunt. (c) Axial T_2-weighted MRI of left congruous homonymous hemianopia due to right occipital lobe encephalomalacia. (d) Axial T_2-weighted MRI of left incongruous homonymous hemianopia due to right parietal lobe arteriovenous malformation. (e) Visual motion perception–related activation as a function of stimulus location before and after task-fMRI training suggest some recovery of visual function. Analysis of a patient with right hemianopia after occipital lobe stroke. Random dot kinetograms were used as visual stimuli. Behavioral performance on a direction-discrimination task was assessed with stimuli presented in either the patient's intact field (ie, stimuli were detected on all three administered high-resolution perimetry tests), blind field (ie, stimuli were never detected), or transition zone (ie, stimuli were detected on only one or two tests). For intact visual field stimuli (top), activation within the contralateral motion-processing area of V5/hMT + is observed and is comparable at baseline and after training (black arrow). For blind field

stimuli (middle), there is bilateral activation of V5/hMT + in the contralateral (white arrow) and ipsilateral (black arrow) hemispheres at both baseline and after training. For transition zone stimuli (bottom), task performance at baseline is associated with bilateral V5/hMT + activation (arrows), as well as perilesional activation (dotted circle). Posttraining shows similar bilateral activation of V5/hMT +, but with a larger network of activation within the occipital pole including visual areas V2/V3. The threshold for significance was set at $P < 0.05$. Colors indicate percentage BOLD signal change. A blue to green gradient represents increasing negative change (−3.75% to −8.00%, respectively), and a red to yellow gradient represents increasing positive change (+ 3.75% to + 8.00%, respectively). Adapted with permissions from Refs. 115, 124.

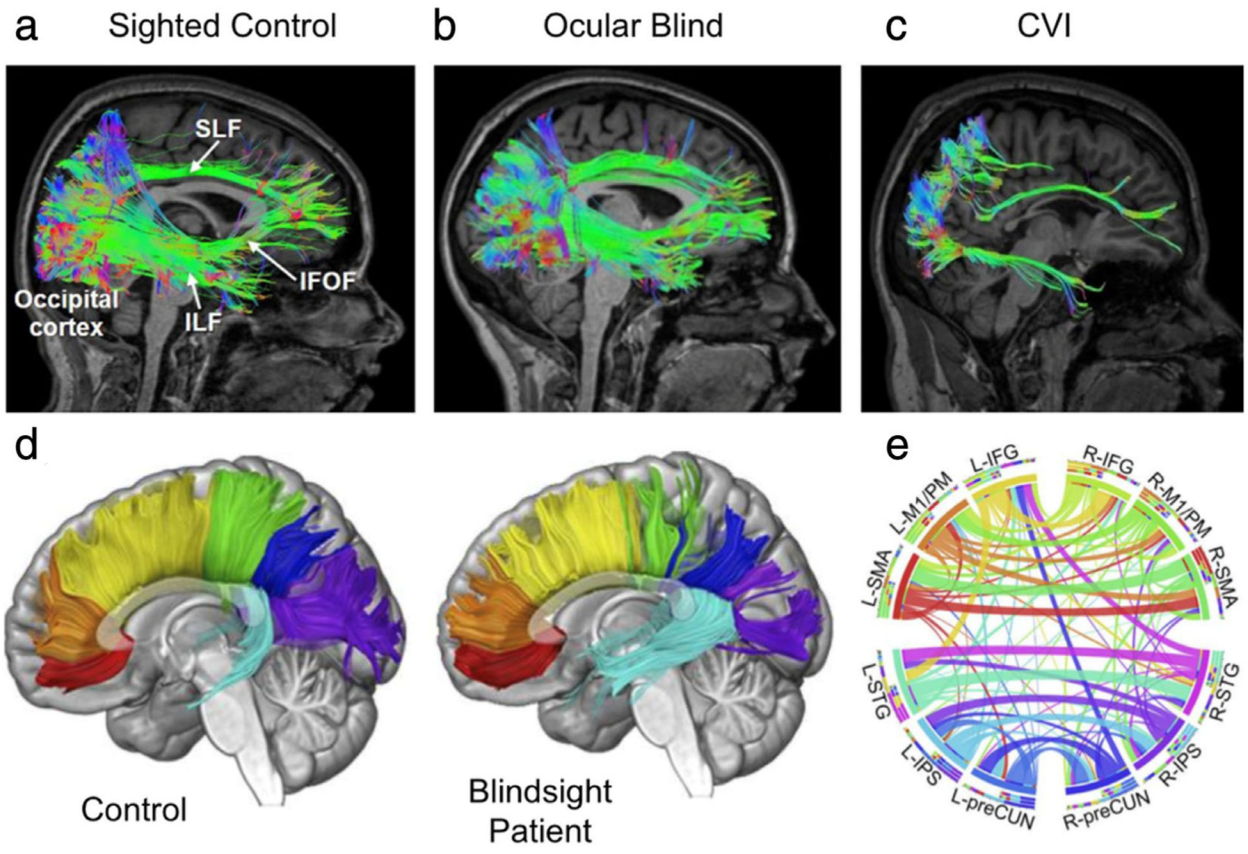

FIGURE 11:

Diffusion tensor imaging of structural connectivity in the cortex and corpus callosum. (a–c) White matter reconstructions (shown in sagittal view) of three main pathways involved in the processing of visual information: the superior longitudinal fasciculus (SLF; the neuroanatomical correlate of the dorsal visual processing stream), inferior longitudinal fasciculus (ILF; the ventral visual processing stream), and inferior fronto-occipital fasciculus (IFOF; mediating visual attention and orienting). Diffusion data was acquired using high angular resolution diffusion tensor imaging (HARDI) for improved delineation of crossing fibers. Pathway reconstructions are shown in a normal sighted control (a), an early ocular blind patient (b), and an individual with cortical/cerebral visual impairment (CVI) and associated periventricular leukomalacia, who has significant visual dysfunction caused by injury to visual pathways and structures during early perinatal development (c). All pathways can be reconstructed in both the control and early ocular blind individuals. In contrast, in the individual with CVI, the SLF and ILF are sparser, and the IFOF cannot be reconstructed. These differences in structural integrity may be related to the observed cognitive visual dysfunctions in CVI. (d,e) fMRI-guided tractography shows connectional, topographic, and microstructural properties of the corpus callosum (CC). Tractographic segmentation (d) of seven callosal fibers based on cortical projections in one representative control participant (left) and one patient who suffered right hemianopia with macular sparing at age 8, following selective destruction of his left striate cortex as a result of traumatic brain injury (right). This arrangement of subdivisions is clearly discernible in the midsagittal cross-section of the CC (as shown) and highly coherent

across patient and age-matched controls. Fibers are color-coded: red, orbitofrontal; orange, anterior frontal; yellow, superior frontal; green, superior parietal; blue, posterior parietal; purple, occipital; and cyan, temporal. Circular representation of the connectional fingerprint associated with functionally (e) defined cortical areas coactivated with callosal clusters of the CC using diffusion-weighted MRI and probabilistic tractography with fMRI. Segments represent different areas and ribbons represent fiber tracts, to clearly assess the relationship between structural and functional brain properties. Connections between areas in opposite hemispheres that did not course through the activated clusters in the CC are not displayed. L = left; R = right; IFG = inferior frontal gyrus; M1/PM = primary motor/premotor cortex; SMA = supplementary motor cortex; STG = superior temporal gyrus; IPS = intraparietal sulcus; preCUN = precuneus. Adapted with permissions from Refs. 120, 121.

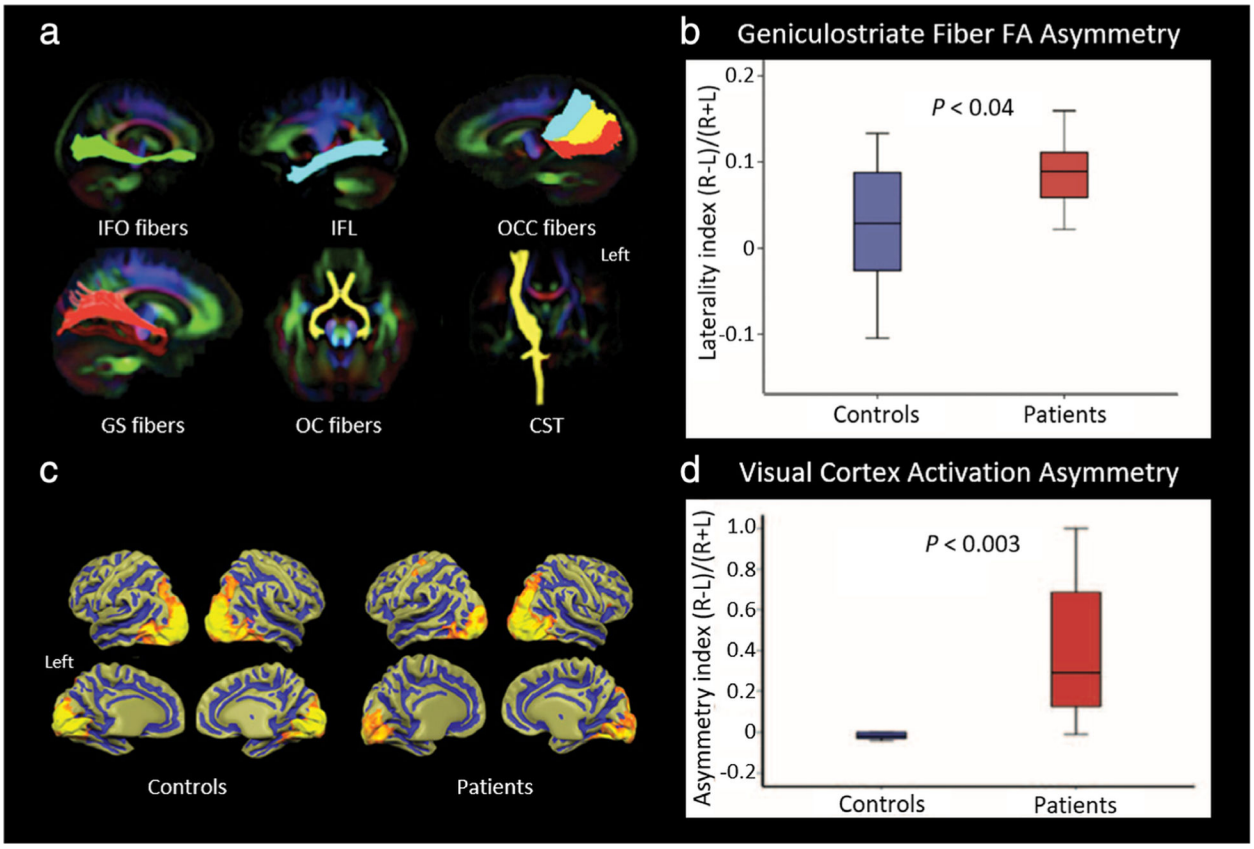

FIGURE 12:

MRI of visual system plasticity following retinal gene therapy. Patients with Leber's congenital amaurosis, a congenital retinal dystrophy that causes severe vision loss early in life, underwent gene therapy via subretinal injection of an adeno-associated virus vector into the superior temporal retina of the right eye, which projects ipsilaterally at the optic chiasm and, therefore, should only affect visual pathways projecting to the right hemisphere. Imaging occurred at least 2 years after gene therapy in these patients, along with demographically-matched control volunteers. MRI was conducted with a 3T scanner using a 32-channel head coil. (a,b) Diffusion tensor tractography. Major fiber tracts between the visual cortex and other parts of the brain, including the inferior fronto-occipital (IFO) fibers, inferior longitudinal fasciculus (IFL), occipital callosal (OCC) fibers, geniculostriate (GS) fibers, and optic chiasm (OC) fibers, as well as the nonvision-related corticospinal tracts (CST) as control fibers, were extracted and superimposed as anatomical regions-of-interest (ROIs) for average fractional anisotropy (FA) calculation in each tract. Fiber bundles were superimposed on a color FA template (a), with the left side of the brain on the right side. Tractography analysis only showed a difference between patients and controls for the GS fibers. A laterality index for average FA along the left and right GS fibers for each group was calculated (b). Patients had a much higher FA along the right GS fibers, and the laterality index was significantly different between groups, suggesting structural normalization of the right hemisphere visual cortex and GS fibers following unilateral treatment. (c,d) Functional imaging of visual cortical activation. Group-averaged fMRI results (c) of high-contrast checkerboard stimuli presented to the right eye of controls and

patients showed symmetrical activation in the hemispheres of sighted controls, in contrast to the asymmetric activation in patients, which had much greater cortical activity in the right hemisphere. Here, the left side of the brain is on the left. An asymmetry index for total volume (number of voxels) activated in the left and right visual cortex was calculated in each group (d). Significantly greater quantifiable activation asymmetry was found in patients compared to controls, further demonstrating unilateral functional plasticity in response to treatment. Adapted with permission from Ref. 125.

TABLE 1.

Summary of Selected Imaging Protocols for the Human Visual System

Anatomy	Pathology	MRI type	Imaging method/sequence	Field strength	Field of view (mm)	Voxel size (mm)	Ref.
Eye/Orbit	Choroiditis	Structural	$T_{1;}$ T_2 SE SPIR	1.5T	80 × 80	0.31 × 0.36 × 2	26
Eye/Orbit	Uveal melanoma	Structural	3D TSE T_1 SPIR; 3D TFE T_1	7T; 9 T	80 × 80 × 40	1.0 × 1.1 × 1.00.8 × 0.8 × 0.8	32
		Structural	Diffusion-weighted TSE	16 T	100 × 100 × 24	1.25 × 1.4 × 2.4	
		Functional	DCE-MRI	17T	80 × 80 × 32	1.24 × 1.5 × 1.5	
Eye/Orbit	Uveal melanoma	Structural	T_1/T_2 3D GRE; T_2 MS Fast SE + SPIR; T_1 3D Fast SE + contrast + SPIR	3T	N/A	0.8 × 0.8 × 0.8; 0.4 × 0.4 × 2.0;1.3 × 2.0 × 2.0; 1.0 × 1.0 × 1.0	35
Eye/Orbit	Retinoblastoma	Structural	T_1 + fat saturation; T_2	1.5T	N/A	0.586 × 0.586 × 2	36
		Structural	RARE; FLASH (ex vivo)	9.4 T; 17.6 T	N/A	0.1 × 0.1 × 0.1;0.06 × 0.06 × 0.06	
Eye/Orbit	Diabetic Retinopathy	Structural/ Functional	DCE-MRI; FLASH	1.5T	N/A	0.39 × 0.39 × 12	40
Eye/Orbit; Visual nuclei	Glaucoma	Metabolic	Single-voxel PRESS MRS	1.5T	12 × 12 × 12	12 × 12 × 12	72
Optic nerve	Healthy	Structural	Diffusion-weighted spin-echo EPI	3T	166 × 41.5	1.3 × 1.3 × 1.3	51
Optic nerve	Multiple sclerosis; neuromyelitis optica	Structural	Readout-segmented echo-planar diffusion weighed MRI	3T	220 × 220	1.1 × 1.1 × 2.9	48
Optic nerve	Traumatic optic neuropathy	Structural	Diffusion-weighted spin-echo EPI	1.5T	220 × 220	0.86 × 0.86 × 5	53
		Structural	T_2 FLAIR	1.5T	240 × 210	0.94 × 0.95 × 4	
Optic nerve/Optic radiation	Glaucoma	Structural	Diffusion-weighted EPI	3T	250 × 250	0.8 × 0.8 × 2	93
Visual nuclei	Glaucoma	Structural	3D BRAVO	3T	256 × 256	1 × 1 × 1; 0.8 × 0.8 × 1.8	65
		Structural	Fast SE PD-weighted	3T	256 × 256	0.8 × 0.8 × 1.8	
Visual nuclei	Normal tension glaucoma	Structural	Readout segmented diffusion-weighted EPI	7T	220 × 220	1.3 × 1.3 × 1.3	67
		Structural	3D MP2RAGE		226 × 240	0.8 × 0.8 × 0.8	
Visual nuclei	Congenital/acquired blindness	Functional	Sparse EPI	3T	N/A	3 × 3 × 3	78
Visual nuclei	Amblyopia	Functional	T_2* GRE	4 T	N/A	3.1 × 3.1 × 3	77
Visual nuclei; Optic radiation	Amblyopia	Structural	T_1 3D fast spoiled GRE	1.5T	240 × 240	0.9 × 1.1 × 1	81
		Structural	Diffusion-weighted EPI			1.9 × 1.9 × 4	

Anatomy	Pathology	MRI type	Imaging method/sequence	Field strength	Field of view (mm)	Voxel size (mm)	Ref.
Visual nuclei; Visual vortex	Glaucoma	Metabolic	Single-voxel PRESS MRS	1.5T	LGN: 13 × 13 × 13; V1: 20 × 20 × 20	LGN: 13 × 13 × 13; V1: 20 × 20 × 20	73
		Structural	3D T_1 FLASH	1.5T	250 × 250	1 × 1 × 1	
Optic radiation	Optic nerve glioma	Structural	Diffusion-weighted EPI	3T	256 × 256	2 × 2 × 2	82
Optic radiation	Multiple sclerosis	Structural	Dual-PD-T_2, postcontrast T_1; FLAIR	3T	220 × 220	0.5 × 0.7 × 2	87
Optic radiation	Amblyopia	Structural	3D spoiled gradient recalled pulse	3T	220 × 220	0.85 × 0.85 × 2	91
		Structural	Diffusion-weighted EPI		240 × 240	1.9 × 1.9 × 3	
Optic radiation	Glaucoma	Metabolic	Single-voxel MRS	3T	20 × 20 × 20	20 × 20 × 20	95
Visual cortex	Pituitary macroadenoma	Structural	3D MP2RAGE	7T	520 × 640	0.7 × 0.7 × 0.7	102
Visual cortex	Hemianopia/ hemispherectomy	Structural Functional	3D MPRAGE EPI	3T	256 × 256	1 × 1 × 1 2 × 2 × 2	99

SE = spin echo; SPIR = spectral presaturation with inversion recovery; TSE = turbo spin echo; TFE = turbo field echo; DCE = dynamic contrast enhanced; MRI = magnetic resonance imaging; GRE = gradient echo; RARE = rapid acquisition with relaxation enhancement; FLASH = fast low-angle shot; PRESS = point resolved spectroscopy; MRS = magnetic resonance spectroscopy; EPI = echo planar imaging; FLAIR = fluid-attenuated inversion recovery; BRAVO = brain volume imaging; PD = proton density; MP2RAGE = magnetization-prepared 2 rapid acquisition gradient echoes; MPRAGE = magnetization-prepared rapid acquisition gradient echo; LGN = lateral geniculate nuclei; V1 = primary visual cortex.